Dissertation
submitted to the
Combined Faculties of the
Natural Sciences and Mathematics of the
Ruperto-Carola-University of Heidelberg, Germany
for the degree of
Doctor of Natural Sciences

Put forward by
Chung Vu Hoang, M.Sc
born in Thanh Hoa, Vietnam

Oral examination: June 23rd 2010

Infrared Spectroscopy of One-dimensional Metallic Nanostructures on Silicon Vicinal Surfaces

Referees: Prof. Dr. Annemarie Pucci
Priv.-Doz. Dr. Maarten F.M. DeKieviet

Infrared Spectroscopy of One-dimensional Metallic Nanostructures on Silicon Vicinal Surfaces – Vicinal silicon (111) surfaces are used as templates for the growth of lead nanowires as well as gold and indium atom chains. The morphology of the Au atom chains was studied by use of Scanning Tunneling Microscopy (STM) and Reflection High Energy Electron Diffraction (RHEED). The In chains were investigated by infrared spectroscopy with the electrical field component of the IR light polarized either parallel or perpendicular to the wires. It is shown that at room temperature, In atom-chains display a plasmonic absorption feature along the chain but not in the perpendicular direction. Furthermore, upon cooling down to liquid nitrogen temperature, a metal to insulator transition is observed. A structural distortion is also confirmed by RHEED. As for the result of Pb nanowires, by means of infrared spectroscopy, it is now possible to control the average length of parallel nanowire arrays by monitoring four experimental parameters that influence on the nucleation density; namely: Pb coverage, evaporation rate, substrate temperature and the surface itself. The system shows an enhancement of the absorption at the antenna frequency in the low temperature regime. This scenario is assigned to the reduction of electron-phonon scattering due to low temperature.

Infrarotspektroskopie an eindimensionalen Metall-Nanostrukturen auf gestuften Siliziumoberflächen – Vizinale Silizium-(111)-Oberflächen wurden als Substrat für das Wachstum sowohl von Blei-Nanodrähten als auch von atomaren Ketten aus Gold und Indium verwendet. Die Morphologie der Au-Atomketten wurde mittels Rastertunnelmikroskopie (STM) und Beugung hochenergetischer Elektronen (RHEED) untersucht. Die In-Ketten wurden mittels Infrarotspektroskopie mit Polarisation des elektrischen Feldes parallel und senkrecht zu den Drähten untersucht. Es wird gezeigt, dass die In-Ketten bei Raumtemperatur eine plasmonische Absorption entlang der Drähte, jedoch nicht senkrecht dazu aufweisen. Weiterhin zeigte sich beim Kühlen zur Temperatur flüssigen Stickstoffs ein Metall-Isolator-Übergang. Mit RHEED wurde dabei auch eine strukturelle Veränderung gefunden. Durch die mit Infrarotspektroskopie gefundenen Ergebnisse für die Blei-Nanodrähte ist es nun möglich, die durchschnittliche Länge von parallelen Nanodrähten durch die Kontrolle von vier experimentellen Parametern zu kontrollieren. Diese sind die Bleibedeckung, die Verdampfungsrate, die Substrattemperatur und die Oberflächenbeschaffenheit. Das System zeigt im Tieftemperaturbereich eine Verstärkuing der Absorption bei der Antennenfrequenz. Diese Beobachtung wird mit der Reduktion der Elektron-Phonon-Streuung infolge der tiefen Temperatur erklärt.

Contents

1. Introduction

Research about one-dimensional (1-D) metallic nanostructures has attracted much attention, since 1-D structures hold novel properties that are closely related to their fascinating optical properties. 1-D metallic structures at the nanoscale also have potential applications since they can broadcast, transmit or receive electromagnetic waves in the optical range which then can be used in nanoelectronics, see [1] and references therein. Further, there has been significant effort to bring them into applications in life science as they exhibit a field enhancement of the electric field at their tip-ends which then might be used to detect vibrational signals of single molecules [2].

1-D structures at atomic scale show a different perspective as they are promising to provide a platform for fundamental research. For instance, 1-D atom wires show a non-Fermi liquid behavior and an instability at low temperatures, the so-called Peierls distortion [3, 4].

Additional to top-down methods in nanostructure synthesis, bottom-up processes of 1-D structures by self-organization processes are attracting a lot of attention as the fabricated structures are more stable and may show high crystallinity [5]. This advantage allows us to study the intrinsic properties of the 1-D structures.

Within the framework of this thesis, 1-D metallic nanostructures made of gold, indium, and lead are fabricated by self-organization methods on silicon vicinal surfaces which serve as 1-D channels for surface diffusion. Their optical properties are investigated by means of infrared spectroscopy.

Because of providing low energy excitations from around 0.1 eV to 1 eV, (mid) infrared (IR) spectroscopy is well suited for the investigation of vibrational features of molecules and free charge carrier excitations. Hence the electronic properties of metallic nanoobjects can be determined without the need of direct contact measurements [6, 7]. IR spectroscopy therefore provides a different insight into the optical properties of nanostructures than spectroscopy in the visible range.

There exists plenty of literature about our method which can be accessed at [8, 9] and references therein.

The chapters of this thesis are arranged in the following way:

1. In chapter 2, there will be a short introduction to the history of silicon vicinal surfaces and optical antenna theory. As the nanoantenna is working at optical frequencies, a new class of antenna theory will be introduced in order to meet this requirement. The antenna extinction cross section of a single nanowire will be considered. In addition to that, a technical issue related to spectrum treating will be mentioned.

2. Chapter 3 is going to deal with the experimental apparatus, setup for the sample holder, and resistive heating to treat the silicon wafer. Since the key problem in the sample preparation is cleaning and getting reconstructed silicon surfaces, details of the experimental procedure will have highest priority in this chapter. Furthermore, an introduction to reflection high energy electron diffraction (RHEED) and scanning tunneling microscopy (STM) will be given, accompanied by some examples performed on Si(111)-7×7 reconstructed surfaces. Details of low temperature experiments will be presented as well.

3. Chapter 4 contains the results, which can be divided into four different parts. Part 1 is going to show the morphological studies on vicinal surfaces. Part 2 displays the nucleation of lead nanowires on such silicon templates, including the observation of *in-situ* growth, tailoring the average length of the nanowires and also the spectroscopic realization of the shape relaxation occurring at the tip-ends of the nanowires. Part 3 contains results of the plasmonic enhancement of lead nanowires at low temperatures, including both experimental results and theoretical estimations. It is will be shown that the observed phenomena is closely related to the reduction of electron-phonon scattering which reduces the plasmon damping at low temperature. Part 4 deals with infrared spectroscopic studies on a well-known structure: indium atom chains (or atom wires in some cases). The anisotropy of the plasmonic absorption of In atom chains at room temperature will be presented under two different excitation regimes of the electric field. The data on the low temperature phase of indium wires is going to be shown, and discussed.

4. In chapter 5, a summary of this thesis will be presented.

2. Basics

2.1. Silicon vicinal surfaces

Probably, the name *vicinal surface* is first used by George Cayley in 1895 in his mathematical paper on surfaces [10]. Up to the 60s of the last century, there were some theoretical works on this interesting problem, starting from [11]. The experiments came later in the beginning of the 80s with experiments on the silicon vicinal surface by means of scanning tunneling microscopy [12]. Since then, the silicon vicinal surface is the most popular investigated to date.

Figure 2.1.1 shows the possibilities to cut the silicon crystal from [111] towards $[11\bar{2}]$ direction to form silicon vicinal surfaces. Herewith only some high miller index surfaces are emphasized: Si(335), Si(557), Si(553) and Si(775). In this work, Si(557) with a miscut angle of 9.45° is used for the experiments of gold atom chains and lead nanowires, Si(111) with an angle of 1° is used for indium atom chains (this surface is not shown in Figure 2.1.1).

Because of having steps which can serve as one-dimensional (1D) channels for the surface diffusion, the silicon vicinal surface is used to synthesize 1D structures made of atoms or wires that are organized by self-assembly, see [3, 14] and references therein.

For the case of metal atom chains, the interest was focused on seeking for the perfect 1-D structure which can exhibit Peierls distortion or spin-charge separation. The former case was first reported by Yeom and co-workers in 1999 [4], the latter case was published in Nature in the same year [15]. In the years after 1999, many research groups had performed experiments to search for the spinon-holon separation effect. In 2006, there were two publications claiming that an evidence for this effect that had been published was not reproducible [16, 17].

In parallel to the interests in atom chains, some significant effort had been paid on fabrication of self-assembled nanowires on vicinal surfaces to investigate the optical properties of the metal nanostructures grown by self-organization processes [5, 18]. This thesis focuses on both issues that were mentioned above.

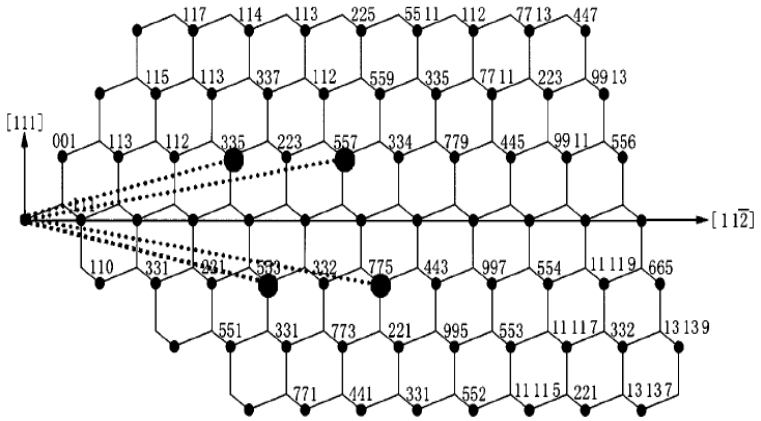

Figure 2.1.1.: A lattice structure of the [1$\bar{1}$0] plane of a silicon crystal. There are some popular vicinal surfaces which can be formed by cutting the crystal in a tilted angle from the [111] direction [13]. In our experiments, Si(557) is used.

2.2. Antenna theory

A surface plasmon is a quasiparticle consisting of collective oscillations of the free electron gas in the metal surface. Probably since the famous contribution by T. Ebbesen in 1998 [19] on the peculiar transmittance of light through subwavelength hole arrays, there has been much interest in the surface plasmon.

Metallic nanowires, when being excited by parallel excitation to the long axis, act as nanoantenna which hold potentials in application. Fundamentally, the plasmonic absorption in the nanoantenna reveals the coupling of the electric field with the surface plasmon of the antenna, leading to a field enhancement of the electric field at the tip-ends of the wires [2, 20]. Taking this advantages into considerations, the promise of nanowires is magnified since they can be used in a wide range of potential applications not only in nanoelectronics, but also in single molecule sensing and many more [21].

In the conventional case of antennas working at radio or microwave frequencies, at the fundamental resonance, the length of an antenna is simply equal to half of it resonance wavelength. The situation is changing for the case of antenna at the nanometer scale since they are working at optical frequencies. The classical antenna theory fails in giving an exact relationship between resonance wavelength and the length of the nanoantenna. The reason is the electromagnetic wave does not reflect perfectly from the antenna but it rather penetrates into the metal. The penetration of radiation into metal gives rise to the collective oscillation (surface plasmon) of free electron gas in

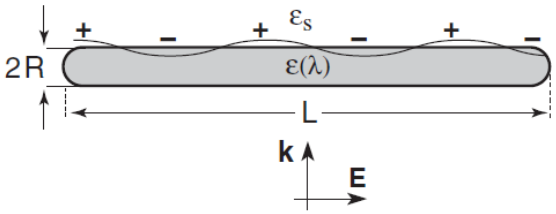

Figure 2.2.1.: A representation of an optical nanoantenna by L. Novotny. The electric field is projected in the long axis of the wire and therefore it creates a polarization of the free electrons in the nanowire. [22].

the nanowires leading to a shorter effective wavelength which depends on the details of nanoantenna and material property [22].

2.2.1. Optical antenna

In 2007, Lukas Novotny gave a simple expression for the optical nanoantenna [22]:

$$\lambda_{\text{eff}} = n_1 + n_2 \frac{\lambda_{\text{res}}}{\lambda_{\text{P}}}, \tag{2.2.1}$$

where λ_{eff}, λ_{res}, λ_{P} are the effective wavelength of the antenna, the wavelength of fundamental resonance, and the plasma wavelength of the material used, respectively. n_1 and n_2 are factors that take into account the diameter and material properties of the wire. Equation 2.2.1 is used within an assumption that the antenna is a homogeneous cylindrical rod with diameter $R \ll \lambda_{\text{res}}$, see Figure 2.2.1.

In comparison to the classical antenna theory, the optical antenna theory offered by Lukas Novotny provides a better accordance to experimental data since it takes into consideration the diameter of the wire and the plasma frequency which is specific for the material used. Within this work, this formula is used to treat the development in length of the nanowires in the *in-situ* growth mode, see paragraph 4.2.

From the practical point of view, to improve the functionality of a nanowire, one has to improve the quality factor Q which is simply defined by the full width at half maximum (FWHM) of the resonance curve. Especially in the case of sensing application, the sharpness of the resonance curve plays an important role in the detection of vibration signal from molecule which is matched with the broad band signal of the nanoantenna [2].

Within this work, the plasmonic resonance of lead nanowires can be treated

as local plasmon. In this case, with the validity of electrostatic approximation[1], F. Wang and R. Shen reported theoretically that, for a given resonance position, the Q factor depends solely on the complex dielectric function of the material but not on the geometry of the structure [23]. The dielectric function of a free electron gas is described by the Drude-Sommerfeld model which takes into account the plasma frequency and relaxation rate of the metal [24].

$$\varepsilon(\omega) = \varepsilon_\infty - \frac{\omega_p^2}{\omega^2 + i\omega\omega_\tau}, \tag{2.2.2}$$

where ε_∞ is the the background polarizability, $\omega_\tau = 1/\tau$ is the relaxation rate of the electrons (τ is the relaxation time) and ω_p is the plasma frequency of the metal which is defined by the density of free electrons and electron effective mass as following:

$$\omega_p = \sqrt{\frac{ne^2}{\varepsilon_\infty m^*}}. \tag{2.2.3}$$

Equation 2.2.2 reveals that for a certain value of frequency, the complex dielectric function of a metal is determined by its plasma frequency and relaxation rate of free electron gas. As such, to make an improvement of the quality factor Q - FWHM possible, one has to get insight into these fundamental parameters of the metal used. In this thesis, section 4.3 will present the effort to deepen the knowledge of this issue.

2.2.2. Treating the resonance spectrum

As will be discussed in Chapter 3, for some instances, the influence of the vibrational signals of water and CO_2 bands make it difficult to determine exactly the resonance positions of plasmonic absorptions. In this work, such spectra can be fitted by Fano functions to describe the resonance curve.

The Fano formula has been introduced by Ugo Fano in 1961 [25], originally to describe the asymmetric resonance of two coupled oscillators by introducing the so-called asymmetric factor. Depending on the coupling regime, the asymmetric factor is varied.

[1] The key criterion of this approximation is the ratio of nanostructure dimensions and wavelength of electric field $L/\lambda \ll 1$

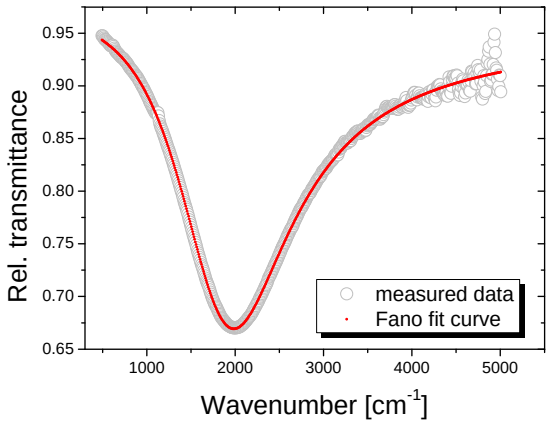

Figure 2.2.2.: An example of a Fano fit curve for a relative transmittance spectrum.

Throughout this work, the Fano function is used as a simple math equation to describe the resonance curve of nanoantenna in the IR. For some spectra with low signal to noise ratio, Fano fitting helps significantly to identify the resonance frequency as well as the full width at half maximum (FWHM) of the curve.

The Fano function is described as following:

$$I(\omega) = I_{\text{const}} + I_0 \frac{\left(1 + \frac{2(\omega-\omega_0)}{a\Gamma}\right)^2}{1 + \left(\frac{2(\omega-\omega_0)}{\Gamma}\right)^2}, \tag{2.2.4}$$

where I_{const}, I_0 are dimensionless fitting parameters, ω_0 is the resonance frequency, Γ is the FWHM of the resonance curve, and a is the so-called asymmetric factor, a dimensionless parameter which defines the asymmetric shape of the resonance curve.

2.2.3. Extinction cross section

The extinction cross section generally is considered as total of absorption and scattering of light from the object. Extinction of a single wire can be calculated if the density of wires is known. The relationship between extinction cross section of a single wire and the corresponding transmittance

of an ensemble of wires is expressed as [26]:

$$\sigma_{\text{ext}} = (1 - T_{\text{rel}}) \frac{n_{\text{Si}} + 1}{2N}, \tag{2.2.5}$$

where σ_{ext} denotes the extinction cross section of a single wire, T_{rel} relative transmittance of the ensemble of wires and N is the nanowire density on the silicon substrate. The presence of refractive index of silicon n_{Si}=3.42 reflects the influence of the polarizability of the substrate on the extinction cross section. Within this work, N can be determined by means of either atomic force microscopy (AFM) or scanning electron microscopy (SEM).

3. Experiments

3.1. UHV chamber and equipment

The *in-situ* experiments were performed in ultra high vacuum (UHV) conditions at a base pressure of 1×10^{-10} mbar. The lowest pressure that could be reached was 8×10^{-11} mbar.

As indicated in figure 3.1.1, the setup consists of a UHV chamber coupled via KBr windows with a Fourier transform infrared spectrometer FTIR Bruker Tensor 27. Details of the configuration of the FTIR components can be found in Figure 3.1.1. The IR radiation was guided from the globar (1) through a small aperture (2) to hit a parabolic mirror. From there, a Michelson interferometer (with planar mirrors (3) and a beam splitter (4)) was used instead of a dispersive element for the IR radiation. The IR radiation then was conducted through a grid polarizer and then focused at the sample position. The IR detector was placed behind the sample in an evacuated detector chamber to record the IR transmittance signals. The data reported in this thesis is measured with a mercury-cadmium-telluride (MCT) detector. A MCT detector provides higher signal to noise ratio in comparison to a DTGS [1] detector. On the other hand, an MCT detector has disadvantages since it has to be cooled with liquid nitrogen to enlarge the energy gap of its effective material, and cooling is stable only for about four hours. Further, to get a precise result, one has to overcome the nonlinearity of its intensity as well.

The surface morphology was monitored by a reflection high energy electron diffraction (RHEED) device. The RHEED setup consists of an electron gun with an initial electron energy of 20 keV and a phosphorescence screen of 8 inches in diameter. The RHEED diffraction patterns were recorded by a CCD[2] camera.

Lead, gold (and indium) were evaporated from alumina crucibles, heated by resistive heating. The evaporation rate (flux) of lead and gold was controlled precisely by a water cooled quartz crystal microbalance [27]. The rate of

[1] DTGS: Deuterated Triglycine Sulfate
[2] The Charge couple device

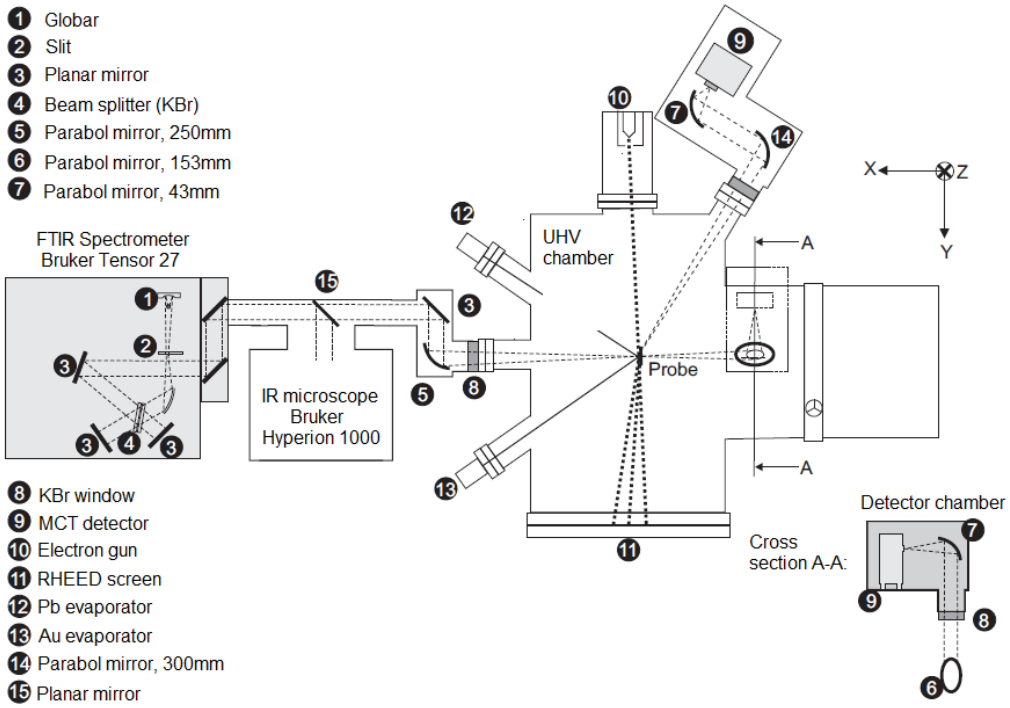

Figure 3.1.1.: Schematic drawing of the UHV system used for FTIR transmittance measurements, plane view. Reproduced from [27] with modification. The infrared microscope and the design for reflectance measurements have not been used within the framework of this thesis.

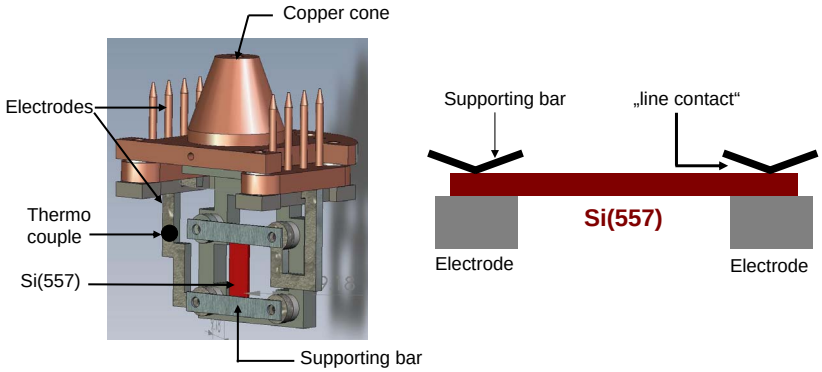

Figure 3.1.2.: An illustration of the sample holder used for mounting the sample, heating by direct current flow, cooling in the low temperature experiments. Reproduced from [29].

indium flux was calibrated by consideration of the phase formation of the $\sqrt{3} \times \sqrt{3}$ reconstruction on the Si(111) surface. It is known that at a surface coverage of 1/3 monolayer of indium, the In-induced phase on Si(111)-7×7 completes the transformation from the 7×7 to the $\sqrt{3} \times \sqrt{3}$ reconstruction [28].

The pressure in the main apparatus was maintained by an ion getter pump and a titanium sublimation pump. A load-lock system is placed at the bottom of the chamber (not shown in Figure 3.1.1) whose functionality is to introduce a new sample into the main chamber without the need of venting. The pressure in the load-lock system was kept at the range of about 10^{-8} to 10^{-9} mbar by a turbo molecular pump.

The silicon sample was mounted in a sample holder as shown in Figure 3.1.2. The external stress was minimized by holding the silicon sample between softly supporting bars where the sample can expand freely upon heating. There were two supporting bars for the sample and they acted also as electrical contacts for the direct heating process. All of the electrodes and the involved components have to be isolated electrically to the cryostat. The copper cone on top of the sample holder was connected mechanically to the cold head of the cryostat. Thereby the thermal energy can be transferred from the sample to the cryostat. The temperature was measured by a chromel-alumel thermocouple (type K) attached close to the sample position as indicated in figure 3.1.2. It is worth to notice that a direct temperature measurement at the sample position was impossible, since the direct contact might cause metallic contamination of the sample.

For the temperature related measurements, the manipulator is cooled down

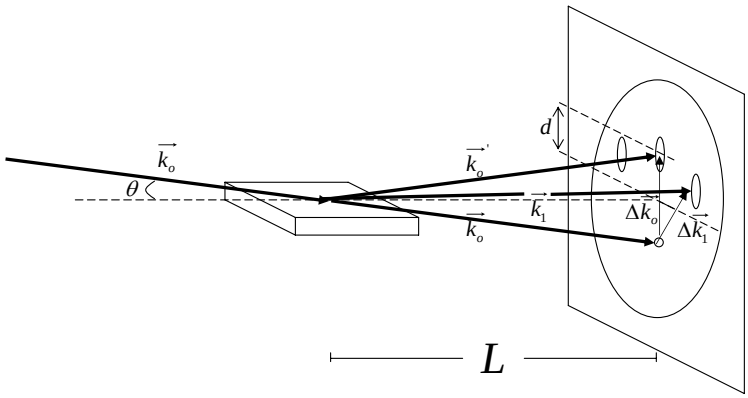

Figure 3.2.1.: A schematic illustration of a typical RHEED setup, consisting of an electron gun, a sample surface, and a phosphorescent screen. The glancing angle of the incoming electron beam is determined from the specification length L of the machine and the distance d between the fundamental spot and the shadow edge of the diffraction pattern. The diffraction patterns on the phosphorescent screen are recorded by a CCD camera.

by liquid helium (LHe). The lowest temperature that could be reached was 23 K at the sample holder and 6 K at the cryostat, respectively. The thermodrift of the sample position upon cooling due to changes of the extension of the cryostat was determined to be about 1.5 mm from RT to LHe temperature. This vertical drift made it highly difficult to measure accurately at the same position during cooling as the entire sample was shifted. To make the *in-situ* experiments possible in spite of that drift, a good sample preparation has to be obtained. The requirement for a good homogeneity in a huge area can be safely met. The details of such sample preparation will be presented in the next text part 3.4.2.

3.2. Reflection High Energy Electron Diffraction

Reflection High Energy Electron Diffraction (RHEED) is a commonly used method for structural analysis. A RHEED setup consists of three major parts: an electron gun for a monoenergetic beam, a phosphorescent screen, and a clean surface as displayed in Figure 3.2.1. Interpretation of the RHEED images is rather complicated and thus RHEED is often accompanied by a Scanning Tunneling Microscope (STM) to check the surface structure. Because of having many scattering events, RHEED analysis needs deep experience in surface treatment and knowledge about the scattering events.

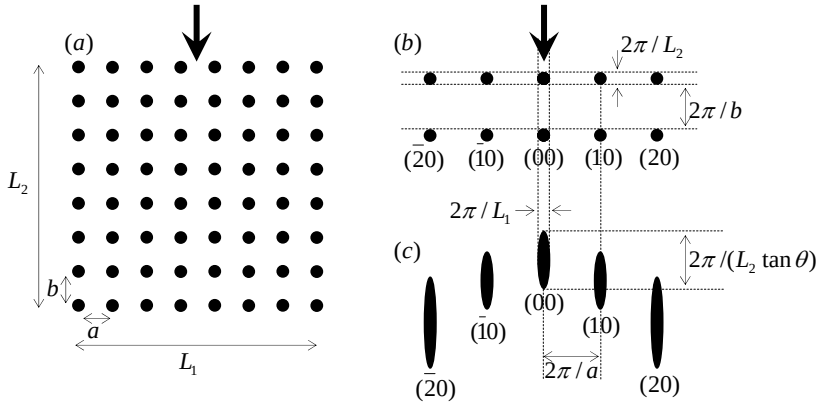

Figure 3.2.2.: Kinematic explanation of the origin of the RHEED pattern. (a) A proposed two-dimensional surface with dimensions L_1 and L_2 with lattice constant a and b. The incident direction of the electron beam is indicated by the arrow. (b) Reciprocal lattice for the arrangement in (a). (c) RHEED construction for (b); the length of the streaks depends on the glancing angle of incident θ [31].

In our setup, the electron energy is set to 20 keV, corresponding to an electron wavelength of 0.087 Å via the relation

$$\lambda = \sqrt{\frac{h^2}{2mE}}, \tag{3.2.1}$$

where h is the Planck constant, m is the electron mass and E is electron energy.

Since the perpendicular penetration depth of electron beam into material is very small, depending on the incident angle θ of the experiment, electrons can be diffracted mainly from the surface. The RHEED technique therefore is useful for surface characterization and monitoring of epitaxial growth [30].

Figure 3.2.2 displays the basics of kinematic RHEED analysis from real surface to the reciprocal space and RHEED patterns. With the lattice constants a and b in the real space, we get $2\pi/a$ and $2\pi/b$ in the reciprocal space. Therefore, in the direction of the incident electrons, one can estimate the lattice constant of the crystal by measuring distance between the diffracting spots on the screen. Of course, this is a rough estimation since deviations come from the optical length of the camera used, and the error of the specification length L of the setup etc. The rough estimation generally helps to find out the relation of the surface superstructure to the fundamental structures of the bulk.

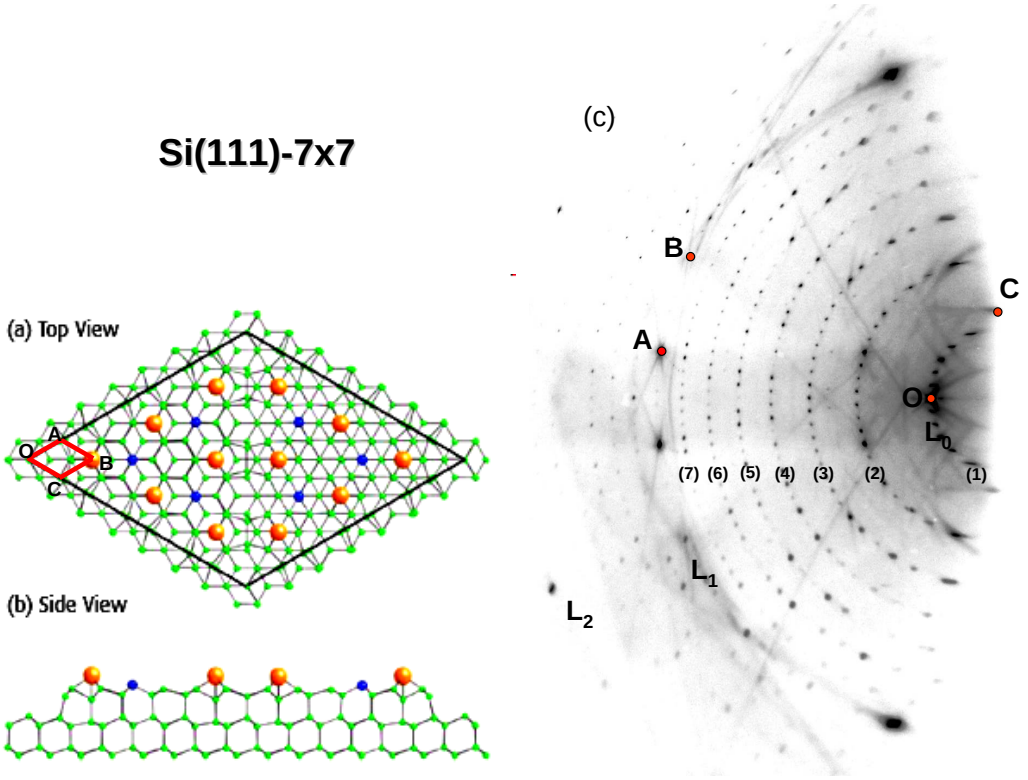

Figure 3.2.3.: RHEED pattern of the Si(111) 7×7 reconstruction: (a) top view of the 7×7 reconstruction for the dimer-adatom-stacking fault (DAS) model [32], reprinted from [33]. The bulk unit cell is indicated as the red section. (b) Side view of the atomic structure of the reconstruction. (c) RHEED pattern of the 7×7 superstructure, incoming electron beam along the long axis of the 7×7 unit cell in (a), electron energy 20 keV, incident angle of ∼1.5°, this work.

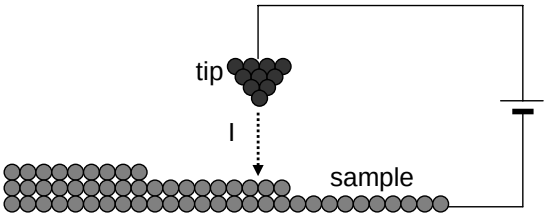

Figure 3.3.1.: A schematic view of a scanning tunneling microscope.

From Figure 3.2.2, for a domain size $L_1 \times L_2$, we see an elongation of the RHEED streaks according to $L_2 \tan\theta$. With a certain incident angle θ, the domain size defines the elongation of the streaks in the manner that the smaller domain gives the longer RHEED streaks and vice-versa.

Figure 3.2.3 shows the RHEED pattern of the Si(111)-7×7 reconstruction (with a 1×1 unit cell in the bulk as a reference) and its atomic structure. Details of the Si(111)-7×7 surface preparation will be presented in the next section.

For a 1×1 unit cell with lattice constant a, after the 7×7 reconstruction the new unit cell has the lattice constant $7a$. Therefore in the reciprocal lattice, 1×1 and 7×7 unit cells are of the size $2\pi/a$ and $2\pi/7a$, respectively. As can be seen from Figure 3.2.3 where the unit cell of 1×1 is marked as OABC, the corresponding unit cell in the Laue zone is indicated in Figure 3.2.3. In the RHEED diffraction, from zero to the first Laue zone (from O to A), there are 7 rings and from O to C, there should be 7 spots. In the content of this work, RHEED is often used as a tool for the distinction of the surface quality and also the presence of the Au and Si chains on the Si(557)-Au reconstructed surface, which will be presented in the next part 4.1.2.

3.3. Scanning probe microscopy

Scanning probe microscopy is a widely used method for surface characterization. It utilizes an interaction between a tip and a sample to image the surface while the tip is scanning spatially over the surface line by line.

Scanning Tunneling Microscopy (STM) and Atomic Force Microscopy (AFM) are used in this work to get information about the surface morphology of the silicon vicinal surfaces and the grown nanowires, respectively. Basically, AFM is more flexible in the practical use, as it can operate with non-conductive substrates. Within this thesis, all of the AFM images have been taken under

ambient conditions, right after transferring the sample out of the vacuum chamber. The AFM is used in two different modes of operation: contact mode and tapping mode, respectively, whose details can be found in [34] and references therein.

STM differs from AFM since it utilizes a tunneling current between a tip and a conductive surface while as in the AFM, the sharp tip is moved over the surface by a piezo element.

Figure 3.3.1 shows the working principle of an STM where the tip is around 1 nm above the surface, the bias voltage is applied, resulting in a tunneling current between the tip and the sample (current direction depends on the bias voltage). The relation between the tunneling current I and the separating distance d of tip-sample can be expressed as [35]

$$I(x, y; V) \propto f(x, y; V)\, e^{-2\kappa\, d(x,y)}, \tag{3.3.1}$$

where $f(x, y; V)$ is the joint density of state (JDOS) of the STM tip and the surface, V is the applied bias, (x, y) denotes the tip position, κ is a decay length which in the simplest model is given by

$$\kappa = \frac{\sqrt{2m\phi}}{\hbar}, \tag{3.3.2}$$

where m is electron mass, ϕ is an average work function of tip-sample. For a typical metal, the value of work function is 4 - 5 eV, κ turns out to be in the range of 1 Å. Thus, when the separated distance changes by 1 Å, the tunneling current drops nearly one order of magnitude. It can be inferred that we can profile hyperfinely the surface with sub-angstrom scale precision.

The other term in equation (3.3.1) reflects the JDOS function, for a DOS of the metallic tip assumed as constant. Therefore, the image contrast of an STM image depends on the electronic configuration of the surface. If the surface is highly conductive, the electron wave function is spreaded out in the entire scanning domain and atomic resolution is hardly to be achieved. On the other hand, for a semiconductor surface (silicon as an example) the electron wave is more localized and therefore a higher contrast can be obtained. In general, to avoid thermal vibration of the lattice (for a better resolution), one has to cool down the sample.

Table 3.1.: *Ex-situ* cleaning materials for silicon wafer in the ultrasonic bath.

Step	Chemicals	time (min)
1	Ethanol	10
2	Deionized water	5
3	Acetone	10
4	Deionized water	5

Table 3.2.: Specification of the silicon wafers used in this work. Low doping level samples for infrared studies. The (557) orientation is used for studies of Pb and Au nanostructures.

Thickness	0.38 mm
Width	5 mm
Length	18 mm
Orientation	(557)
Type	P
Polished	both sides
Resistivity	0.5 Ωcm

3.4. Sample preparation

3.4.1. *Ex-situ* cleaning

In order to produce highly regular step arrays on silicon, one has to overcome a variety of obstacles, since irregular or bunched steps may occur.

Prior to transferring the Si wafer into UHV, the sample was prepared by ex-situ cleaning with ethanol, acetone and deionized water in an ultrasonic bath. This process removed dust from the wafer, but not the natural silicon dioxide layer. All manipulations of the sample were conducted carefully with clean ceramic tweezers to avoid metallic contamination of the wafer. Details of the chemicals, cleaning time for each solvent and the order of the cleaning process are listed in table 3.1.

In the last step (table 3.1), cleaning in deionized water for 5 min helps mechanically to remove remaining C-H groups of former cleaning steps from the wafer. It helps avoid the formation of silicon carbide on the silicon wafer while the later heat treatment in the vacuum.

The Si(557) vicinal substrates were produced by Toshiba Crystal with both

sides polished. Table 3.2 shows the specification of the Si(557) samples used for the experiments. In particular, for the use of infrared experiments, low doping silicon wafers are used since they provide a higher transmittance as the absorption range of free charge carriers is restricted to the far infrared.

As substrate for the experiments with indium atom chains, the Si(111) vicinal surface was cut with a small angle of 1° from the [111] direction. The experimental procedure for treating the sample is as explained above for Si(557).

3.4.2. Flashing

For flashing, the sample was mounted on the holder in between two electrodes without any stress. This stress-free state enabled the sample to withstand short heating pulses of direct current without damage. To fulfill such requirements, the supporting bars were designed in a way to reduce the friction between them and the sample. The contact pads were made in groove shapes, producing there *line* contacts with enough force to hold the sample. With this design, a silicon sample can be used for many experimental runs without the need of replacements.

Flashing is a special process for sample cleaning under UHV conditions. Its original purpose is to remove the natural silicon dioxide from a surface. In flash cleaning, the sample is rapidly heated by a direct current. The current is oriented parallel to the steps in order to avoid step bunching [36].

As can be seen from Figure 3.4.1, there is a linearity between heating current and the sample temperature in the *log-log* plot. The temperature was read-out by an optical pyrometer with emissivity set to 0.4. Its error was around 30 K. The calibration procedure was performed on a test sample which was heated without consideration of the pressure in the apparatus. The calibration result was used as a standard data sheet for the treatment process for the samples having similar dimensions. Of course, the errors arising from the optical pyrometer might cause a serious effect on the surface treating, but thanks to the phase transformation from 1×1 to 7×7 occurring at 830 °C, we could optimize the heating process by calibration of the optical pyrometer.

After being introduced into the main apparatus via the load-lock system, the silicon wafer was heated to 600 °C for about 20 hours. This pre-heating is used to outgass the wafer and the relevant parts of the massive sample holder. Pressure in this initial step was controlled to be better than 10^{-9} mbar. This process was stopped at the final pressure of 2×10^{-10} mbar.

Figure 3.4.2 shows the heating diagram that has been used to treat the sample in UHV after the initial heating. The wafer was first heated up

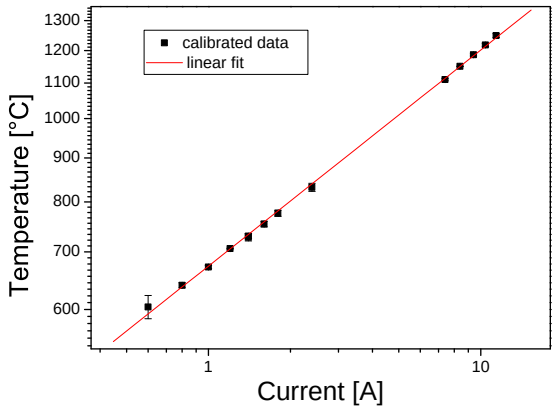

Figure 3.4.1.: Temperature calibration with a silicon test sample. We found a linearity between wafer temperature and heating current in the *log-log* plot. The sample temperature was recorded with an optical pyrometer. For the temperature values below 900 K, an extrapolation is needed to get the corresponding heating current.

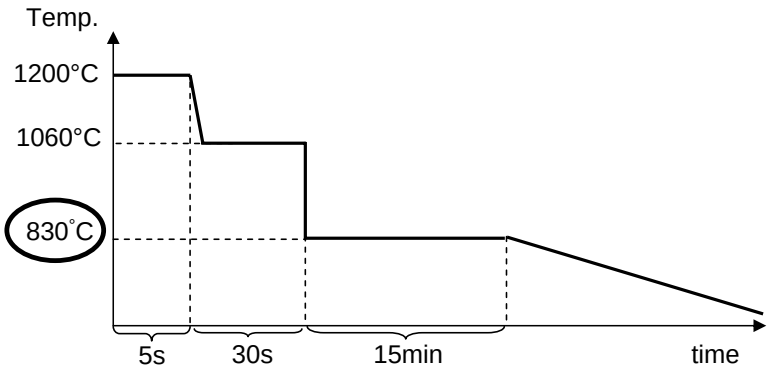

Figure 3.4.2.: Heat treatment diagram applied for flashing of Si samples in UHV.

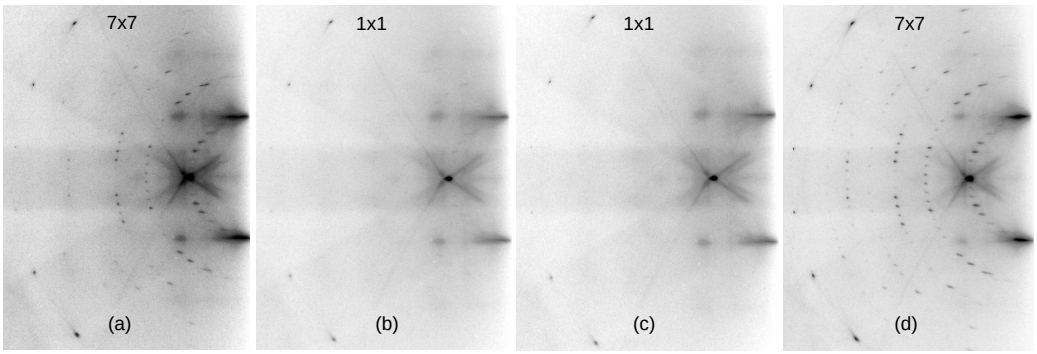

Figure 3.4.3.: RHEED pattern from the phase transition from the 1×1 to the 7×7 superstructure.

several times to 1200 °C by heating pulses for 5 s. This flashing was applied to remove the native silicon dioxide and the residual silicon carbide from the surface. Within 30 s the sample was then cooled to 1060 °C at which the step structures are most stable [37]. Subsequently, the sample was quenched from 1060 °C to 830 °C and annealed there for 15 minutes and then slowly cooled down to RT.

The most critical step in the treatment procedure is to quench the surface from 1060 °C to 830 °C and to anneal at 830 °C. By quenching, the formation of the silicon carbide is avoided which can be produced on the fresh silicon surface at a temperature range from 1060 °C to 900 °C [38]. The annealing at 830 °C is used to complete the full-transition from the 1×1 to the 7×7 reconstruction and to enlarge the domain size in which the 7×7 reconstruction is stable [39]. As stated above, 830 °C is the temperature of the phase transition of Si(111) surface, and this value can be controlled precisely by electron diffraction.

Figure 3.4.3 shows the phase transition from the 1×1 to the 7×7 superstructure on the Si(111) surface. At figure (a), the temperature was slightly lower than 1030 °C, the co-existence of the 1×1 and 7×7 characters is observed where the fundamental spots of 1×1 have several spots of 7×7 in between. When the surface temperature is higher than 1030 °C, only the 1×1 spot remains (b) and stays there if the temperature did not change (c). The recovery of the 7×7 phase was achieved again by lowering the temperature over the transition point. As reported by Xu *et al* [39], this transition is a second order transition and therefore it is not necessary to take care of latent heat for maintaining the full transition. It is believed that annealing at a constant heating current at 830 °C provides very large and stable domains, which will then be a key parameter for the preparation of the nanowire arrays with good lateral homogeneity.

Table 3.3.: Heating current the silicon wafer, achieved temperature from optical pyrometer used for the standard procedure of substitute preparation .

Temperature [°C]	Heating current [A]	Heating time
1200	13	5 s
1060	11.5	within 30 s
830	2.4	15 min
600	0.72	7 min
350	0.1	—

Table 3.3 presents the corresponding heating currents of flashing which are also used for the fabrication of atom-chains on vicinal surfaces. For the case of gold atom chains, Au was deposited onto a surface kept at 600 °C, annealed there for 7 minutes, followed by slow cooling to RT. In case of indium atom chains, the substrate was kept at 350 °C during In deposition and then slowly cooled down afterwards. All of the processes were monitored successfully with RHEED.

3.5. Measurement procedure

3.5.1. Relative transmittance measurement

There are two very common measurement geometries used in infrared spectroscopy: reflectance and transmittance modes. The reflectance measurements provide the information about the absorbents on the surface. The measurements in the transmittance mode give us another manner to investigate the surface with normal incidence. For this geometry, the $\overrightarrow{k}$ vector is perpendicular to the surface, but the electric field is parallel to the surface. Hence, depending on the purpose, a polarizer can be used to measure in two different excitation regimes: electrical field is parallel to the wires or perpendicular to them.

Figure 3.5.1 presents the measurement procedure which was mainly used in this work. The left image: a schematic illustration of the transmittance configuration with vacuum as a reference. $T_0(\omega)$ is a single beam spectrum, measured from the empty channel (vacuum), $T(\omega)$ is the signal with sample. The relative transmittance is retrieved by dividing the sample measurement to the empty channel one.

The image on the right shows an explanation of the measurement in reality,

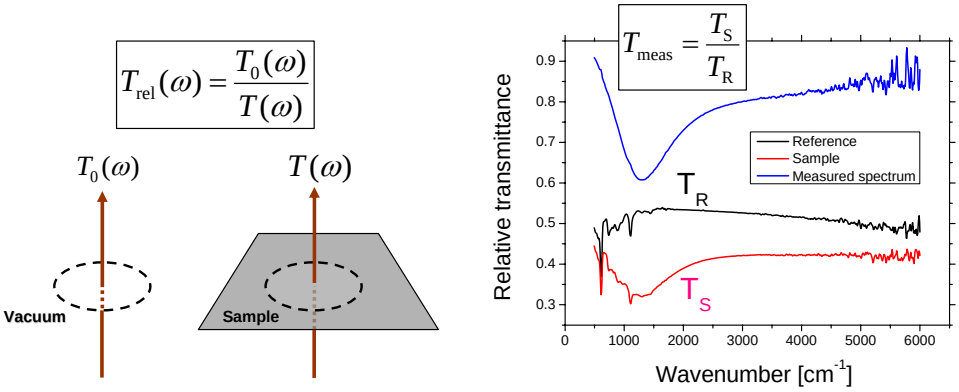

Figure 3.5.1.: Measurement procedure of the transmittance geometry. The details of the experiments can be found in the text.

each spectrum $T_S(\omega)$ or $T_R(\omega)$ is measured with the procedure as shown in the left image. The spectrum of the nanowires $T_{meas}(\omega)$ is achieved by dividing the sample spectrum by its corresponding reference.

The above configuration was used to avoid the instability of the surrounding conditions such as the variation of CO_2 and H_2O compositions in the optical path, the small temperature variation of the main apparatus etc.

In case of *in-situ* experiments, the blank substrate was measured right before the metal deposition in the manner presented above. The relative transmittance spectra were then recorded continuously during metal deposition. In that case, the first *in-situ* spectrum displayed the 100 % line which revealed the stability of the system.

3.5.2. Measurements at low sample temperature

As mentioned above, our setup is equipped with a helium cryostat. The cooling procedure was performed by pumping liquid helium[3] directly into the manipulator. The lowest temperature that could be reached was 6 K at the cryostat and 23 K at the position of the sample holder, as indicated in Figure 3.1.2. The temperature measurements were performed with the temperature reference at liquid nitrogen temperature.

Before performing the low temperature experiments, test runs were performed for checking:

1. The homogeneity of the sample over the lateral shift of the cryostat due to temperature. As written above, the spatial drift of the cryostat was

[3]LHe - liquid helium

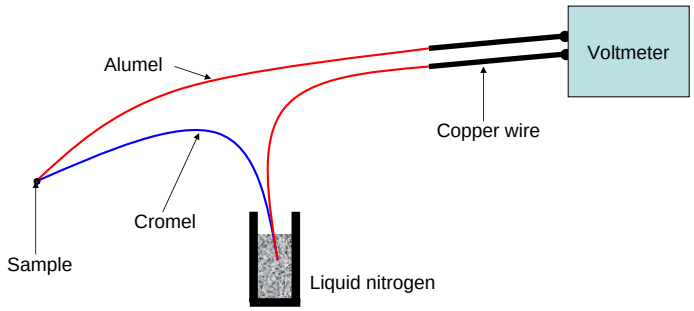

Figure 3.5.2.: Thermocouple for temperature measurement at low temperature.

determined to about 1.5 mm. Within this distance, the resonance curve showed no change in the spectral shape but only a small deviation in the resonance strength of about 0.3 %. This value was proven to be by far smaller than the change resulting from the physical properties of the nanowires.

2. There is no shift of the plasmonic absorption frequency during cooling.

3. There is no change in the morphological features of the nanowires due to cooling.

The test experiments allowed to determine that the temperature gradient between sample and cryostat during cooling is much bigger than during heating from LHe temperature. From that, it is worth to notice that the temperature measurement during heating up from LHe temperature is more reliable than during cooling. All of the experiments showed in this work were done by *in-situ* measurements of the nanowires during heating from LHe temperature.

The thermovoltage at the sample position was retrieved as following:

$$V_{\text{sample}} = V_{\text{LN}_2} + V_{\text{read-out}}$$

where V_{sample} is the thermovoltage at the sample, V_{LN_2} is the reference voltage at liquid nitrogen temperature $-5.829\,\text{mV}$ and $V_{\text{read-out}}$ is the read-out thermovoltage by the voltmeter.

The read-out thermovoltage at the sample position was compared to the standard table of the data sheet which was supplied by the NIST [4], to find out the actual temperature at the sample.

[4]National Institute of Standards and Technology, The USA

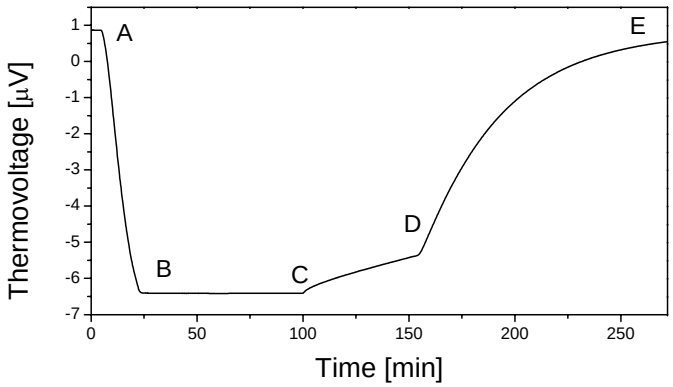

Figure 3.5.3.: Thermovoltage recorded with the thermocouple (type K) attached close to the sample position indicating the temperature evolution during cooling with LHe. From point A, the system started to be cooled down and the LHe pumping stops at B. From B to C was the waiting time for getting the actual equilibrium state. From C, the *in-situ* measurements were being conducted, the system was heated by adsorbing thermal energy from the outer space. At point D, compressed air was conducted through to heat up the cryostat. The heating duration stopped at point E.

Figure 3.5.3 brings out the actual process that had been done within one run of the low temperature experiment, followed by the temperature evolution. In total, it took about 4 hours for one run, including cooling from RT to LHe, waiting for stability and heating from LHe to RT. Point A corresponds to RT and point E to 280 K.

In particular, the *in-situ* measurements stop at point E at which the sample temperature is 280 K. Longer measurement were impossible since the experiments have then been performed for 2.5 hours. Within such a long duration, the instability of the system comes into play and the spectra were not reliable as there were undesired signals in the spectra arising from the composition variation in the optical path.

Figure 3.5.4 displays the two-phonon absorption feature of the blank silicon substrate versus temperature variation. It is shown that the wafer shows higher transmittance at lower temperature.

For the two phonon absorption peak centered at 610 cm^{-1}, a monotonic decrease of the transmittance peak was obtained.

For the *in-situ* measurements, the matching between the reference and sample spectra had to be fulfilled absolutely. The relative data are the obtained by dividing the sample to reference spectra, therefore the results should not contain any peaks related to the two phonon absorption.

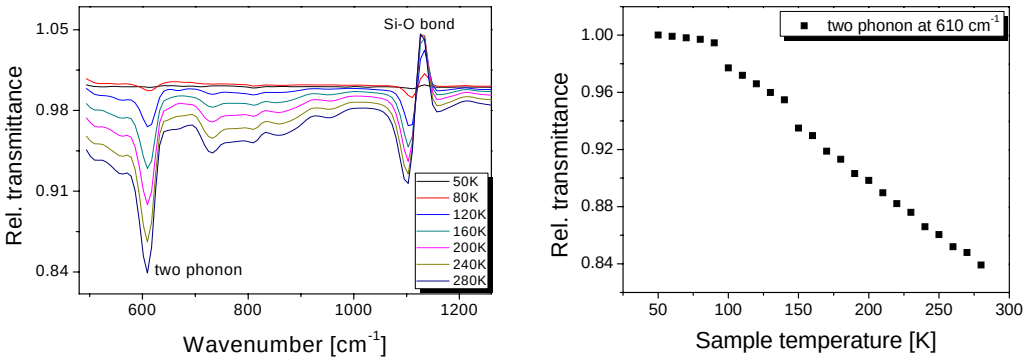

Figure 3.5.4.: Two phonon absorption feature of a bare silicon wafer due to the temperature variation. Left: the normalization of the relative transmittance of the sample at various temperatures to the spectrum at 50 K. Right: the development of the transmittance versus temperature of the two phonon absorption peak centered at 610 cm^{-1}.

4. Results and discussion

4.1. The silicon vicinal surface

According to the sample preparation as shown in Chapter 3, the standard cleaning process was applied to fabricate the silicon vicinal surface with different inclined angles. Herewith in this chapter, a morphological investigation of the Si(557) surface will be presented with the help of the scanning tunneling microscope - STM. This work has been performed in the Maria Curie-Skłodowska University, in the research group of Prof. Jałochowski [40].

4.1.1. The Si(557) step structures

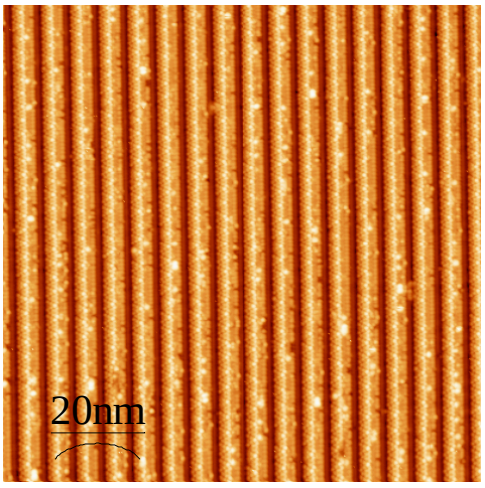

Figure 4.1.1.: A 100 nm×100 nm STM image of the Si(557) surface after flashing and annealing with the standard procedure which was explained in figure [heat process]. The image was recorded at room temperature with a tunneling current of 0.2 nA and a sample bias of -2.193 V.

Figure 4.1.1 shows the as fabricated Si(557) surface, captured at RT with a tunneling current of 0.2 nA and a bias voltage of -2.193 V. The highly regular

arrays of steps were produced with perfect grating-like structure. The steps were atomically straight up and well-separated.

As pronounced in the experimental procedure, the post annealing time and temperature play a major role in the developing of the long-range 7×7 reconstruction. The quenching from 1060 °C to 830 °C avoids the step tripling and freezes the steps. The long annealing time at 830 °C ensures the full transition from 1×1 to 7×7 reconstruction.

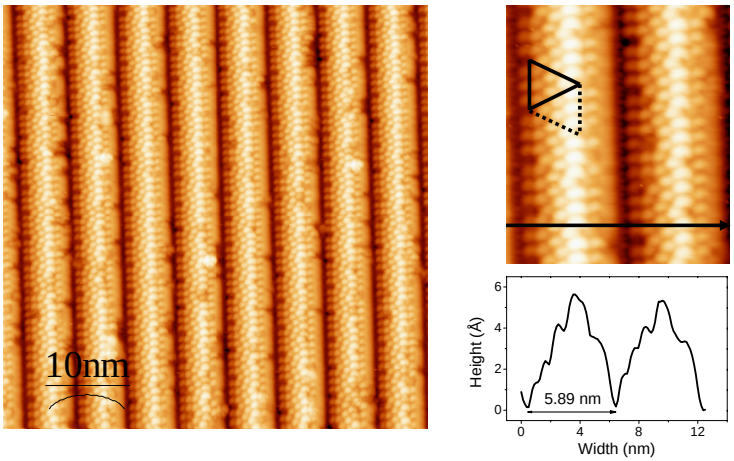

Figure 4.1.2.: A 50 nm×50 nm STM image of the Si(557) surface, recorded with tunneling current 0.2 nA and bias 0.578 V. On the right and side: detail and height profile of the image. The black triangular denote the halves of the 7×7 unit cell on the terrace. This grating-like surface shows a periodicity of 5.89 nm.

Figure 4.1.2 presents another STM image of the same surface but with higher magnification. This filled-state image clearly indicates the presence of a long-range 7×7 reconstruction, but only halves of 7×7 unit cell were presented. The reason for that comes from the off-cut angle of the silicon wafer. The smaller the angle is, the larger the 7×7 areas are. As can be seen from figure 4.1.2, the height profile perpendicular to the steps shows that the periodicity of the as synthesized surface was about 5.89 nm.

It was demonstrated by Kirakosian *et al.* [41] that the periodicity of the unreconstructed step structures is $p = 5.73$ nm. The reason for this discrepancy between the predicted periodicity and measured one can be attributed to either the dynamic of the surface reconstruction or the technical problems of STM tip calibration [1] as well as the precision of the miscut angle

[1] STM tip should be calibrated with standard structure such as Si(111)-7×7 to avoid the discrepancy during experiments.

of the silicon wafer.

The inset of figure 4.1.2 also shows the smeared-out steps. One can clearly see that with the same scanned parameters, the atomic resolution had been achieved in the 7×7 cell but not at the step edges. This observation can be attributed to the metallic nature of the silicon steps in which the electron wave functions are propagated along the chains instead of localized at the individual atoms. It is in agreement with the well-documented fact that the reconstructed silicon surface has metallic silicon dangling bonds [42]. Therefore, the joint density of states (JDOS) of the tip and sample is also not localized while scanning over the steps. This consequence influences on the smeared out observation at the step edges.

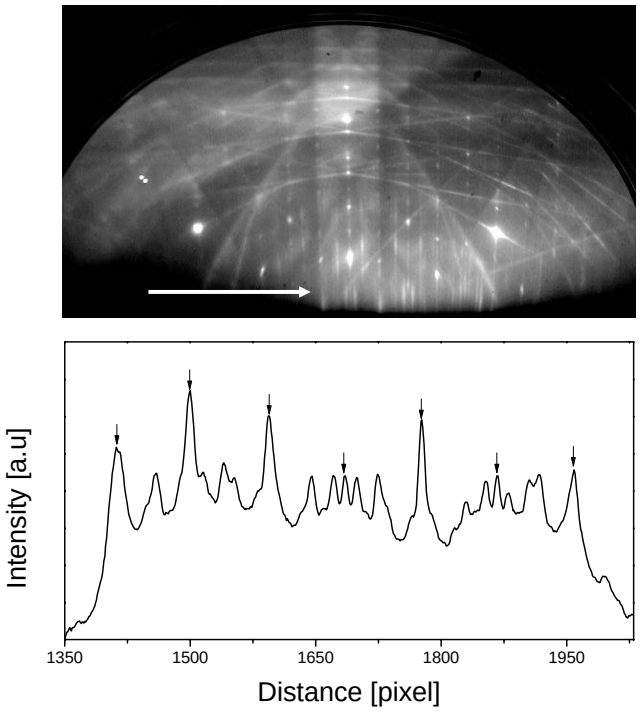

Figure 4.1.3.: A RHEED pattern of the Si(557) surface and its intensity profile. Electron beam was projected in the step down direction, perpendicular to [110] orientation, as indicated by the white arrow. The intensity profile is plotted versus distance to indicate the 1×1 and 7×7 reconstructed features in the surface. In the profile, the arrows indicate the 1×1 of the silicon layers underneath, but the diffraction peaks in between them show the 7×7 character of the surface. Taken with 20 keV, 1.3° of incidence.

Figure 4.1.3 presents a typical electron diffraction pattern of the Si(557)

sample. The incoming electron beam was in the step-down direction.

In comparison to the RHEED pattern of Si(111) flat surfaces in which all of the diffraction features have spot-like shapes, Si(557) shows in figure 4.1.3 diffraction streaks instead. The reason for this streak-like shape is that the step structures on the silicon surface shortened the domain size of the 7×7 in the incident direction of electrons. Hence the width of the step structures define the elongated spots that had been seen in the streak shape on the screen. Besides, the picture shows very high intensity of the background with some smeared out Kikuchi lines and one Kikuchi bar.

The Kikuchi bar (or so-called envelope in some documents) helps to determine the fundamental streaks caused by the 1×1 unit cells of the silicon layers of the bulk crystal beneath the surface. Within the Kikuchi bar, one can find the specular spot in the center and two main streaks at the edges of the envelope.

In the plot of the profile analysis, between the fundamental streaks caused by 1×1 that are marked by arrows in figure 4.1.3, one can observe the minority streaks. There are 6 weaker streaks in between two 1×1 main streaks. From this observation, it is proven that the 7×7 reconstruction has already been present in the structure.

In practice, the 7×7 only appeared if the postannealling procedure was strictly followed to set for the full transition. If the quenching procedure was applied from 1200 °C to RT, only 1×1 fundamental streaks could be obtained. In that case, the surface looked like an amorphous layer with extremely weak and unclear diffraction. It is worth to notice that the recovery of the surface can be re-established again by annealing the surface in the right procedure as paragraphed in the previous chapter.

4.1.2. Au atom-chains on Si(557)

Gold atom-chains on silicon have drawn much interest in the last few years. The reason is documented in Chapter 2 and references therein.

As explained in the previous chapter 3, gold atom chains are formed on the Si(557) by depositing one fifth monolayer of gold onto the substrate followed by post annealing and slowly cooling down to RT. As a result, every unit cell of the bare substrate is occupied exactly by one gold atom as reported by Robinson *et al.* [14]. Also, as reported by these authors, the metallic nature of this atom chains origins mainly from the gold atom chains but not from silicon chains or silicon plains [14].

There are two different approaches to fabricate gold chains by self -assembly: the first method was explained in chapter 3, where the silicon surface is

heated during gold deposition, the second method utilizes the surface at room temperature for gold deposition but followed by a heating sequence at 600°C for few minutes. Both of them need to have high temperature for the gold atoms to move and reconstruct the surface.

Bennewitz *et al.* [43] assumed that the thermal relaxation of the adatoms for the surface reconstruction can be described simply by the activated diffusion. The temperature dependence of the vibration frequency $\nu(T)$ is displayed in term of activation energy:

$$\nu(T) = \nu_0 \ \exp\left[\frac{-\triangle \mathrm{E}}{\mathrm{k_B}T}\right]. \tag{4.1.1}$$

Where the attempt frequency ν_0 is in the range of lattice vibrations, typically of $\nu_0 = 10^{13}\,\mathrm{s}^{-1}$. At temperature 450 K, as inferred from [44], $\nu_{475\mathrm{K}} = 1\,\mathrm{s}^{-1}$, therefore the activation energy on the silicon surface can be estimated as:

$$\triangle \mathrm{E} = \mathrm{k_B}\,T \ln(\frac{\nu_0}{\nu}) = 1.18\,\mathrm{eV}. \tag{4.1.2}$$

The vibration frequency at RT turns out to be $\nu_{300\mathrm{K}} = 10^{-8}\,\mathrm{s}^{-1}$, which is far smaller than the value at 475 K. This value tells us that the surface temperature strongly influences at the surface reconstruction and that the surface adatoms at RT are immobile, in comparison to transition temperature.

Figure 4.1.4 presents a morphological view of the Au-Si(557) surface. As can be seen from the figure, the small inset indicates the as synthesized gold clusters without annealing. The surface shows the disorder on the backbone of the pristine silicon steps.

Figure 4.1.4 clearly shows the role of the heat treatment for gold decoration. Without being heated, the deposited amount of gold can just form small and disordered clusters instead of parallel atom chains. It is clear that the heating performance at 600 °C gives rise to surface diffusion and therefore the gold atoms can move on the surface to choose the preferred positions.

The bright spots that were distributed randomly on the surface seen in figure 4.1.4 originate from silicon adatoms, as reported by Kang *et al.* [45].

In theory, the system looks rather complicated since it consists of not only the gold chains but also silicon chains, both of them are presence within one terrace [13]. As indicated in figure 4.1.5, the silicon and gold chains are parallel to each other. On one hand, gold chains have the same periodicity

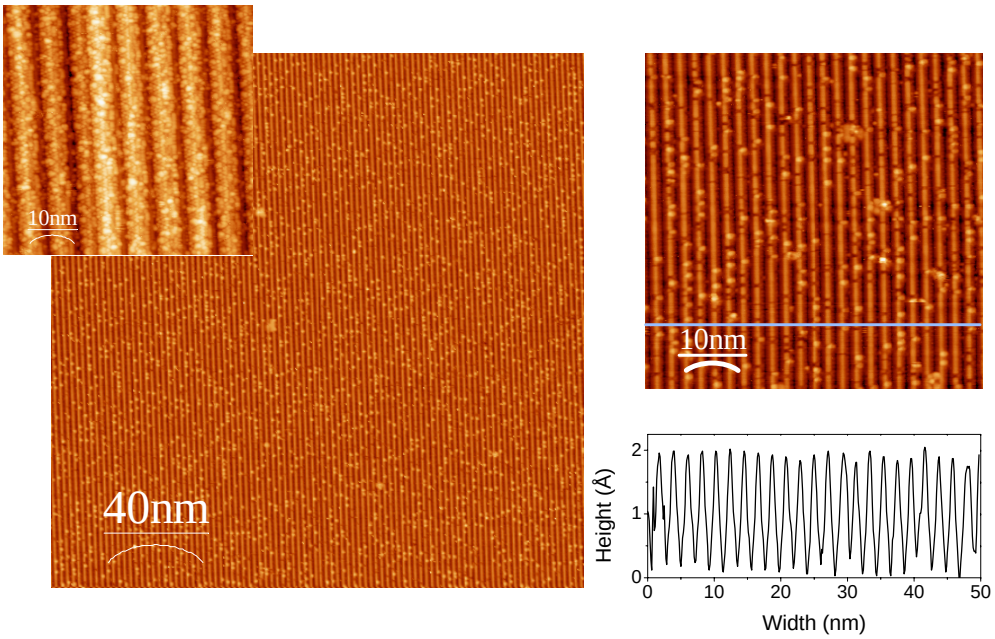

Figure 4.1.4.: A morphological illustration of the Au-Si(557) with height profile crossing the gold chains. The small inset shows the as-deposited Au clusters on the cleaned Si(557), without annealing. The others show the morphology from the same sample but after being annealed at 600 °C for 7 min and a height profile along the blue line. The Au-induced grating-like structure has periodicity of 2.1 nm. The images were recorded at room temperature with the tunneling current 0.2 nA .

with the silicon layer underneath but on the other hand, silicon chains show a doublicity with those of gold. In addition, in one terrace, a silicon plane is also presence nearby.

In practice, Krawiec *et al.* [46] claimed the existence of the double non-equivalent chain structure on one terrace in the Au-Si(557) by STM and *ab initio* simulations. They observed both experimentally and theoretically the existence of this double chains on the terrace. By varying the tunneling current from emptied to filled states modes, both the gold and silicon chains are visible under STM. So far, there is no electron diffraction measurements on this double chain structure.

Figure 4.1.6 shows a typical RHEED diffraction pattern of the Au-Si(557) surface together with STM measurements of the corresponding surface. The STM measurements were performed in Lublin and the electron diffraction was done in Heidelberg with the same sample preparation as indicated in the experimental Chapter.

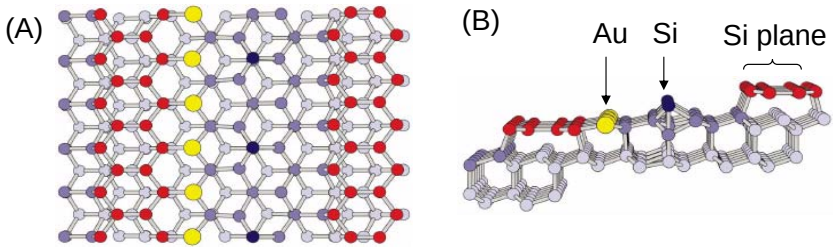

Figure 4.1.5.: An atomic structure visualization, reproduced from [13]. (A) The top-view of the Au-reconstructed structure, where yellow balls denote the Au atoms, black balls for the silicon atoms in the top-most layer, gray ones are for the silicon atoms bounding to the surface and light gray balls for the bulk silicon atoms. (B) The cross-section of the system perpendicularly to the chain direction.

The intention for my STM measurements was the observation of the double non-equivalent chains which is similar to the results by Kraviec *et al.* [46]. Looking at figure 4.1.6, picture (b) and (c) had been taken at the same position but with different bias voltages. Picture (b) with bias -1.794 V shows the filled-state mode where the gold chains are visible, on the other hand, picture (c) with +1.794 V bias indicates the visibility of the silicon chains in the empty-state mode. A height profile analysis along the silicon chains show the periodicity of $2a$ where a is the lattice constant of the bulk silicon. The position of the bright protrusions made of silicon adatoms located in between gold and silicon chains, can be seen when we switch the direction of tunneling current, insets (b) and (c).

Picture (a) and (d) show the RHEED diffraction pattern and the intensity profile along the direction of the incoming electron beam (indicated in the box). In the RHEED pattern, very sharp and strong diffraction spots are visible. Within the Kikuchi bar, the two main diffracted spots of 1×1 are obtained, meanwhile, in the middle area there is one sharp spot of the gold structure. In picture (d), one can easily see that all of the Au spots have the same distance to the 1×1 spots . This is a clear evidence that the diffraction from the gold decoration is supported by the 1×1 underneath, it means that the lattice constant of the gold structure is equal to that of the silicon, a.

Having a closer look at the RHEED pattern along the chain direction, one can see exactly that in between two main spots caused by gold chains, there is a small streak. These streaks are distributed equally along the chains direction, according to the intensity profile in picture (d).

The reliability of the profile analysis depends strongly on the camera used. It is worth to notice that in the direction indicated by the white arrows in the

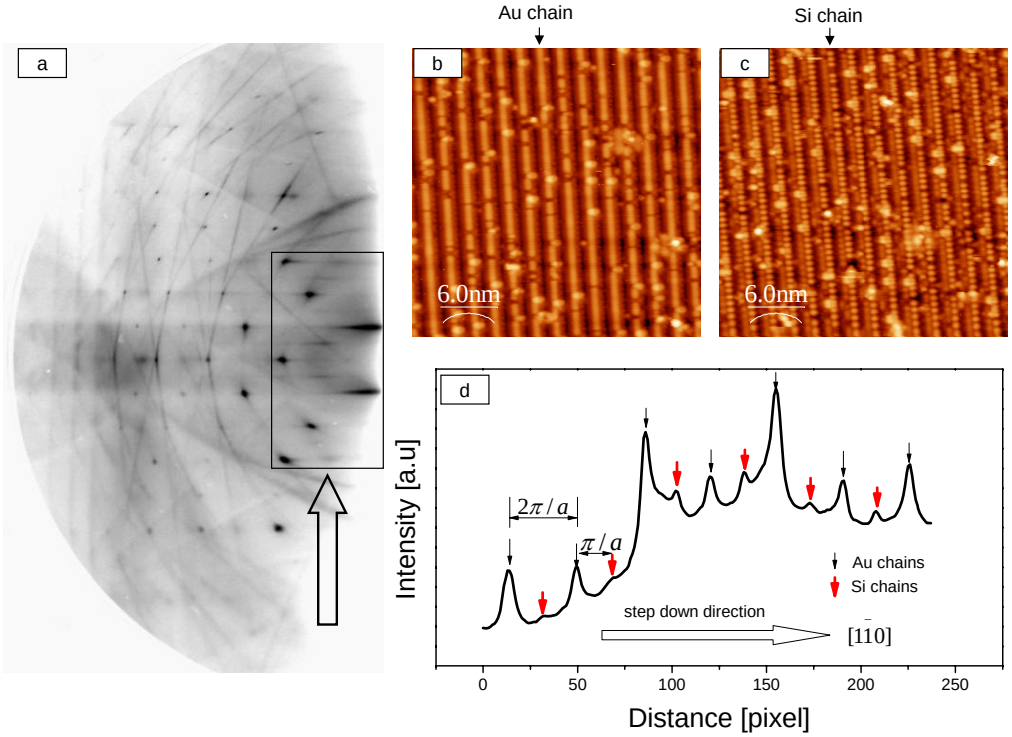

Figure 4.1.6.: The co-existence of the Au and Si chains within one terrace with different periodicity. (a) A typical RHEED pattern of the Au-Si(557), electron beam was projected perpendicularly to the chain direction. (b) and (c) STM images with the same position, scan size 30 nm×30 nm and tunneling current 0.2 nA but different bias voltages: -1.794 V for picture (b) and +1.794 V for (c) accordingly. (d) The intensity profile of (a) with two kinds of diffraction peaks, separated equally. The black arrows denote the signal from Au chains and red arrows for Si chains.

RHEED pattern, the image is not distorted too much in comparison to the perpendicular direction. Therefore the separation distance between diffracted spots gives the information about the lattice constant along this direction reliably.

Along this interchain direction, the equal distribution of the above streaks give the lattice constant in the reciprocal space $\pi/2a$ because the distance between two fundamental spots is π/a. It is an indication that in the real surface, the structure has the periodicity of $2a$, where a is the lattice constant of bulk silicon. In agreement with theoretical prediction by Crain *et al.* [13], and STM observation by Kraviec *et al.* [46], this result obtained with the electron diffraction gives another insight into the coexistence of the non equivalent chains, made of gold and silicon.

4.1.3. Infrared spectrum of gold chains

In general, an anisotropy of the conductivity is expected to be seen optically as it was observed by electron photoemission spectroscopy or scanning tunneling microscopy. There exists plenty of studies on gold chains on the silicon vicinal surfaces such as Si(335), Si(557) [3, 16, 13] and Si(111)5×2 reconstruction [47, 48].

Also, in the beginning of this project, special focus had been paid to investigate the fundamental aspect of the anisotropy in the optical conductivity of the gold atom chains in the infrared.

In fact, it was not possible to observe an anisotropy in the infrared. The reason for that comes from the electronic structure of the gold atom chains that was reported by several research groups, as explained below .

Hasegawa and co-workers reported on the anisotropy of the conductivity via the direct contact measurements [49]. Their results at room temperature showed that the conductivity of Au-Si(557) in the chain parallel direction is three times higher than in the perpendicular direction. This value is much lower than for other substrates. For instance, in case of indium atom chains a ratio of 60 had been obtained [50]. Also, a comparison of the two surfaces which have similar electronic structures: Au-Si(553) and Au-Si(557) had been conducted and reported that surface conductivity along the chains of Au-Si(553) is about 9 times higher than Au-Si(557) [51].

Furthermore, a comparison of defect density between different vicinal surfaces such as Si(553), Si(335), Si(557) and Si(775) by Crain *et al.* revealed that Au-Si(557) has highest defect density [13]. As mentioned above, Kang *et al.* reported that those defects are silicon adatoms which arise from the dynamic process of surface reconstruction [45]. Of course, defect density in such structures depends on the sample preparation, but it helps in general to understand the electron transport occurring in the structures.

Okino *et al.* reported on the above issue by using four point probe method in combination with STM experiments [51]. They assumed that the silicon protrusions act as insulator defects. Hence, they divide the gold metal atom chains into smaller segments in which electrons can move freely. Figure 4.1.4 shows that the average distance from protrusion is about few nanometers. Under the excitation of electric field parallel to the steps, the plasmon can be formed within such the short chains but there will be no signal observed, as reported similarly by Moresco *et al.* [52].

For the electronic structure, Crain *et al.* reported on the band structure by photoemission spectroscopy [13]. Their result reveals that there is no surface states at the center of Brillouin zone that does not allow any optical

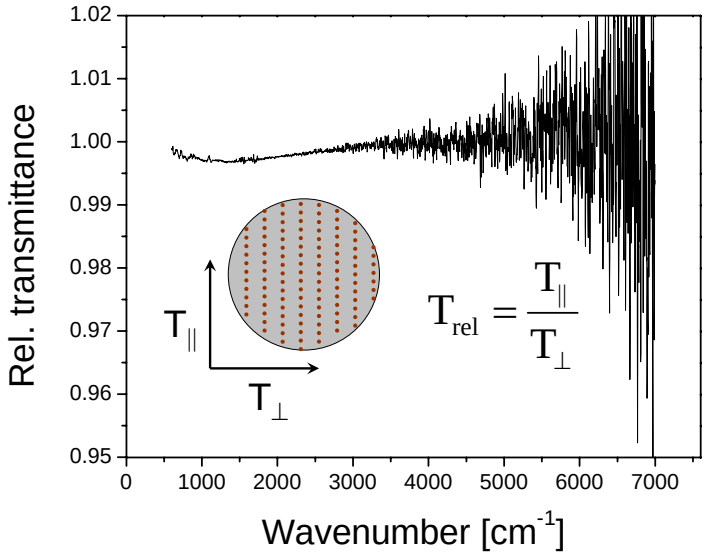

Figure 4.1.7.: Relative transmittance infrared spectrum of gold chains on Si(557). The relative spectrum was derived by dividing the relative spectrum of Au chains in the chain direction ($T_{\parallel}$) over the corresponding spectrum in the interchain direction ($T_{\perp}$), as shown by inset. Each individual spectrum had been accumulated for 6000 scans, resolution of 8 cm^{-1}, and took about 20 minutes.

transitions caused by infrared.

Figure 4.1.7 shows the experimental IRS data on gold chains on Si(557). The spectrum indicates the absolute transparency of the gold chains in the both directions, except a slight decrease of transmittance at low frequencies. This small change can be attributed to the instability of the narrow band MCT detector since there was a long duration of time between the two spectrum.

In conclusion, by combining the electron diffraction and scanning microscope, the double non-equivalent atomic chains had been observed. The silicon and gold chains are present within one terrace, the gold chains have the periodicity of a meanwhile silicon chains have $2a$ instead. The gold chains exhibit an absolute transparency in the infrared range.

4.2. Nucleation of lead nanowires

Spectroscopic studies on the length development of Pb nanowires on the Si(335) vicinal surface have been achieved in our group, see a preceding work by Klevenz *et al.* [18]. In the present work, Si(557) templates were utilized instead of Si(335). In comparison to the Si(335) vicinal surfaces, the Si(557) surface provides a more stable step structure since each of its terraces consists of halves of the Si(111)-7 × 7 unit cell, see experimental chapter 3 for details. The grown nanowires on the silicon vicinal surfaces act as nanoantenna in the infrared range [2] which can be fully understood by using the optical antenna concept [22].

The purpose of this section is to show:

1. The ability to control the average length of the nanowires by governing the nucleation density from very beginning stage. There are four experimental parameters found, namely: the evaporation time, the evaporation rate, the substrate temperature, and the diffusion energy of lead atoms on the surface.

2. The shape relaxation towards equilibrium of as-synthesized wires. Since the development in length of the nanowires is a far-from-equilibrium process [53], the as-synthesized Pb nanowires start to reshape towards equilibrium when the nucleation stops. This shape relaxation was achieved at the tip-ends of wires leading to shorter wires but better crystallinity. The role of so-called corner-rounding diffusion is discussed.

3. Upon cooling, a strong increase of resonance extinction of the nanoantennas is observed at various Pb coverages from 2 ML to 10 ML. By comparison to theoretical estimations, it is clear that this temperature-related enhancement is due to the reduction of electron-phonon scattering.

4.2.1. Length development of lead nanowires

Morphology of nanowire arrays

The morphology of the as-synthesized nanowire arrays was investigated by means of AFM. Figure 4.2.1 shows a typical AFM picture of 10 ML of Pb grown on the Au-Si(557) vicinal surface.[2] The image was taken right after

[2]This experiment has been performed without having the control by the RHEED pattern. Therefore the surface quality was not as well defined as it is described in the experimental chapter 3. Since this data shows a systematic result including morphological and spectroscopic studies, it is used to serve as a guidance for the growth scenario.

the transfer of the sample into ambient conditions. The scanning direction was perpendicular to the long axis of the wires. As can be seen in Figure 4.2.1, in the entire scanning area, the nanowires are aligned perfectly along the steps of the substrate (direction $[1\bar{1}0]$ of the Si(557) surface). Only few lead islands are present which do not show a high aspect ratio.

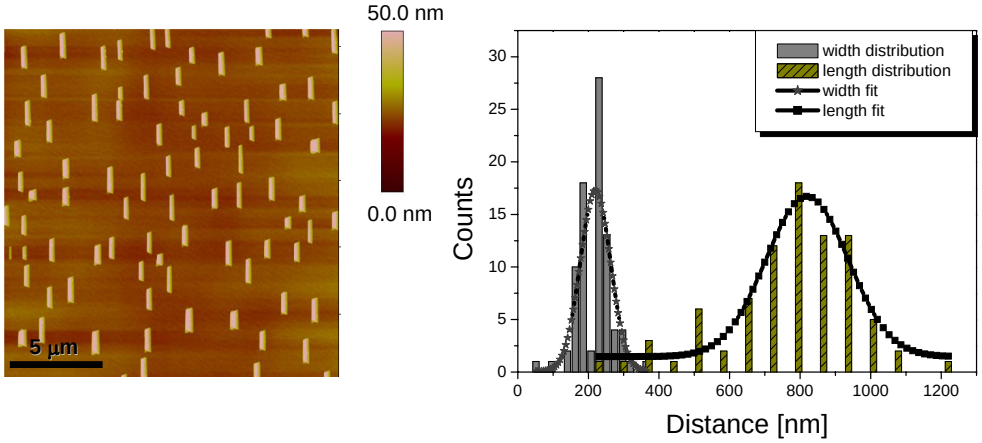

Figure 4.2.1.: AFM image of 10 ML Pb nanowires on Au-Si(557), taken right after transfer of the sample from UHV to ambient conditions, captured in tapping mode. The scanning direction was perpendicular to the wires. The inset in the middle shows a couple of wires with higher magnification. The figure on the right shows the length and width distributions of the nanowires, data taken statistically from the AFM image on the left side. It shows that the nanowires are about 820 nm in length, 220 nm in width and 32 nm in height.

As reported previously by M. Jałochowski and E. Bauer, such macroscopic wires are single crystalline and have a triangular cross-section with the two main plains [100] and [111] [54].

As can be seen in Figure 4.2.1, the wires have very sharp tip-ends. They were grown on a wetting layer consisting of an amorphous layer of lead. By the use of LEEM[3], Jałochowski claimed the existence of a transition point at 1.3 ML where the nanowires start to grow on that wetting layer [54].

Interestingly, the experiments of Pb films on Si(111)-7×7 also show the transition point at 1.3 ML. By performing scanning tunneling spectroscopy (STS) on lead islands grown on the Si(111)-7×7 surface, Zhang *et al.* found that this wetting layer is already conductive [55]. This peculiar surface conductivity might give rise to the difficulty of the experimental investigation since the wires are somehow connected to each other. At low temperature

[3]LEEM - Low Energy Electron Microscope

experiments, the issue even can become more serious because of the increase of metallic conductivity at low temperature due to the reduction of electron scattering, leading to the difficulty of treating the nanowires individually.

Having a look at Figure 4.2.1, one can easily identify the random walk positions of the nanowires in the whole captured area. An analysis of the dimension distribution of the nanowire arrays is displayed on the right hand side. The fit curve of the distribution was treated by the log-normal distribution function [56] and gives an average length of about 820 nm and an average width of 220 nm. The distribution in height was obtained by the software *Gwydion*[4] [57] to be about 32 nm.

In Figure 4.2.1, full width of half maximum (FWHM) of the width distribution curve is $\sim$ 100 nm $\pm$ 30 nm while that of the length curve is $\sim$ 250 nm $\pm$ 30 nm. This means that the (relative) length distribution is more narrower than the (relative) width distribution, indicating that the nanowires are more uniform in length rather than in width. It is worth to notice that the morphological analysis with AFM had been done in the ambient air, therefore, there will be errors in the AFM measurements due to the influence of oxidation effect and water on the lead nanowire surface. Also, although having such effects, the nanowires which had been removed some days from vacuum still showed fundamental resonance close to the original values taken in vacuum. See Appendix.A

IR measurements

Transmittance IR measurements were performed *in-situ* in order to investigate the length development of nanowires. First, a reference spectrum of the bare silicon substrate was measured[5]. Subsequently, during Pb deposition onto the blank substrate, the relative transmittance spectra were recorded continuously.

Figure 4.2.2 shows the development of the relative transmittance spectra versus time of lead deposition. The first spectrum corresponding to 0 ML reveals a 100 % line[6], where there was no lead on the silicon substrate. The following spectra up to 10 ML with the field of the incoming light polarized parallel to the wire display the real-time evolution of a resonance peak shifting to lower wavenumbers during lead deposition.

From optical antenna theory [22], it is known that there is a relationship between antenna length L and its resonance frequency ω_{res}. For a full

[4] *Gwydion* is an open source software which is widely used for the analysis of scanning probe microscopy measurements.

[5] See Experimental chapter for details of the measurement procedure.

[6] 100 % line also reveals the stability of the system right before the experiment

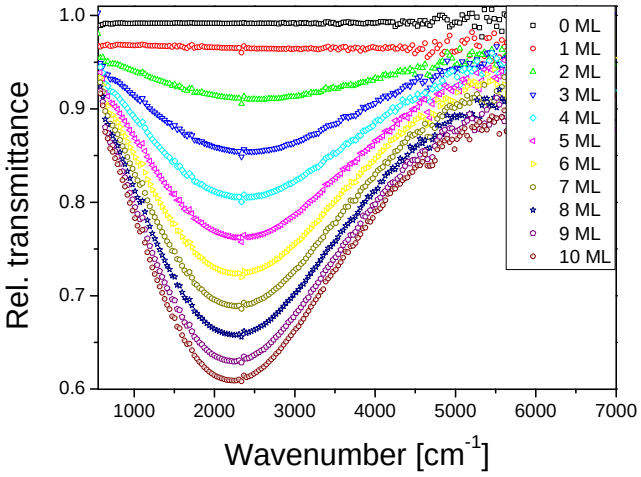

Figure 4.2.2.: IR *in-situ* spectra during deposition of lead. The electric field was parallel to the long axis of the wires. Only selected spectra are shown, ranging from 0 ML to 10 ML. Variation of the CO_2 composition in the optical path caused a signal located at 2300 cm^{-1} in the spectra.

understanding of the antenna resonance in the optical range, one can now express the fundamental resonance by taking into account the influence of the shape and of the material of the nanowires. The simple relationship between length and fundamental resonance wavelength of a nanowire which has been derived by L. Novotny [22] is recalled:

$$2L = \lambda_{\text{eff}} = n_1 + n_2 \frac{\lambda_{\text{res}}}{\lambda_{\text{P}}}. \tag{4.2.1}$$

where n_1 and n_2 are two factors that take into account the radius of a cylindrical wire and λ_{P} is the plasma wavelength which is a specification for the material of the nanoantenna.

Because $\omega_{\text{res}} = 1/\lambda_{\text{res}}$, we have:

$$L = \frac{1}{2}(n_1 + n_2 \frac{\omega_{\text{P}}}{\omega_{\text{res}}}), \tag{4.2.2}$$

where ω_{res} is the frequency of the fundamental antenna resonance.

The simple expression in equation 4.2.2 brings out the conclusion that the shift of the resonance peaks to lower frequencies (smaller energy) indicates that the nanowires are getting longer.

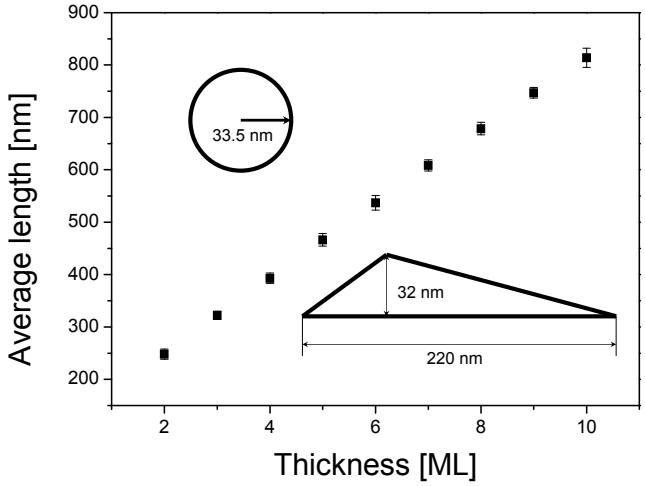

Figure 4.2.3.: Average length of Pb wires estimated from equation 4.2.1 versus Pb coverage. The effective radius was assumed to be 33.5 nm at a film thickness of 10 ML and smaller for lower coverages as described in the text. The insets show the conversion from triangular into circular cross section.

Looking at equation (4.2.1) with some approximations[7] for the convenience in calculating procedure, it can be rewritten as following [22]:

$$L = \pi R \left[13.74 - 0.12 \frac{\varepsilon_\infty + 141.04\,\varepsilon_S}{\varepsilon_S} - \frac{2}{\pi} + 0.12 \frac{\omega_P}{\omega_{res}} \frac{\sqrt{\varepsilon_\infty + 141.04\,\varepsilon_S}}{\varepsilon_S} \right], \tag{4.2.3}$$

where R is the radius of the nanowire, ε_∞ is dielectric constant of the vacuum and ε_S is that of the silicon substrate, ω_P is the plasma frequency that is material specific and ω_{res} is the resonance frequency of the nanowire.

For the comparison of the average length determined by AFM with that determined by the Novotny formula, the dielectric constant of silicon used is $\varepsilon = 11.7$ and the plasma frequency of lead is $\omega_p = 62000\,\mathrm{cm}^{-1}$ [58]. Equation (4.2.3) therefore can be expressed as:

$$L = \pi R \left[-3.82 + \frac{25831}{\omega_{res}} \right]. \tag{4.2.4}$$

The cross section of our nanowires is triangular [54]. In order to be able to use the Novotny approximation, the triangular cross section is converted into

[7] See Chapter 2 for more details.

a circular cross section. The conversion is performed by matching the cross section of the two different shapes. Two small insets in Figure 4.2.3 show how an equivalent radius of circular cross section is converted for the case of 10 ML.

As can be achieved from the AFM data of Figure 4.2.1, for a coverage of 10 ML, R is assumed to be 33.5 nm. For 2 ML, R is measured (not shown) by AFM and converted to be 12.6 nm. The development of average radius of wires versus coverage is assumed to be linear.

Figure 4.2.3 shows a plot of the length development of the nanowire arrays of which the morphology and the relative transmittance have been shown in Figure 4.2.1 and 4.2.2, respectively. As can be seen in Figure 4.2.2, the absorption peak of CO_2 makes it difficult to determine the precise minimum of transmittance. Therefore only selected spectra are considered to be plotted in Figure 4.2.3. The growth of nanowires started from a coverage of 1.3 ML of Pb and was stopped at 10 ML, ending up with an average length of about 813 ± 30 nm. There is a very good accordance between the length determined by AFM (820 nm) and that determined by infrared spectroscopy with the help of the concept of optical nanoantenna (813 nm).

For comparison, we can calculate the average wire length from the classical antenna theory whose equation describes the antenna relationship as following:

$$L\,[\mathrm{nm}] = \frac{\lambda_{\mathrm{res}}\,[\mathrm{nm}]}{2\,n_{\mathrm{eff}}}, \tag{4.2.5}$$

where λ_{res} denotes the resonance wavelength and n_{eff} the effective refractive index of the surrounding media. In our case, it is assumed to be:

$$n_{\mathrm{eff}} = \sqrt{\frac{1 + n_{\mathrm{Si}}^2}{2}} = 2.52. \tag{4.2.6}$$

In the classical expression the average length of the nanowire arrays therefore is estimated to be about $\sim 890\,\mathrm{nm} \pm 30\,\mathrm{nm}$. The deviation between the two methods is about 9.5 %. The Novotny theory shows a better accordance since it takes into account the diameter of wires, and also the plasma frequency which is specific for the material used.

The nucleation process of the Pb nanowires at room temperature was started via forming a wetting layer with the thickness of 1.3 ML. Beyond this first initial stage nucleation and aggregation of the Pb wires were developing. Looking at Figure 4.2.2, for the Si(557) surface, already at 2 ML a resonance peak was obtained at a frequency of $2500\,\mathrm{cm}^{-1}$, corresponding to an average

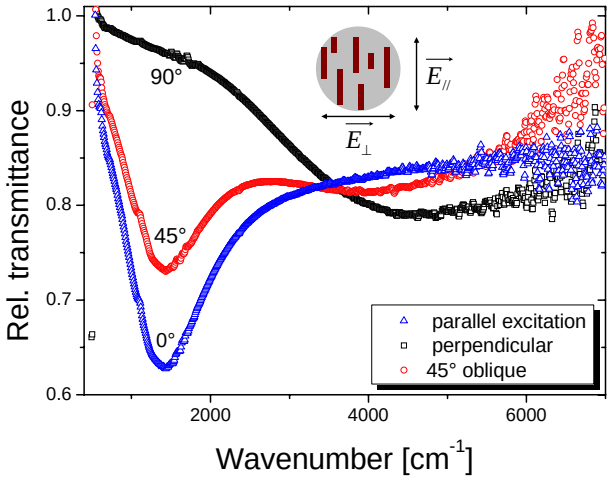

Figure 4.2.4.: Influence of the polarization of the electric field of the incoming light on the plasmonic absorption of 10 ML of nanowire arrays on Si(557).

length of about 250 nm. Hence, in that case, it is worth noticing that only 0.7 ML of Pb contributed to the resonance, indicating that there existed wires that are very long and have a very high aspect ratio.

Figure 4.2.4 shows the influence of the orientation of the electric field on the resonance of the wires. The reference spectra were taken on the blank silicon substrate with corresponding polarization. In case of an excitation with an electric field parallel to the wires, a fundamental mode is achieved located at around 1400 cm^{-1}. In case of perpendicular excitation, the antenna absorption is no more present, but a broad peak that is related to the width of the wires is obtained. When the polarizer was rotated by 45°, the superposition of plasmonic absorption in length and width of wires is present. The fundamental antenna mode has the same resonance frequency but smaller absorption strength.

4.2.2. Tailoring of the average length

Getting full ability to tailor average length the nanowires fabricated by the self-organization method is one of the novelty of this work. In the experimental point of view, the reproducibility of the experiments reflects the reliability of the experimental apparatus.

At the first glance, the main influences on the average length of the wires might depend simply on either the coverage (shown in Figure 4.2.2) or the substrate temperature which defines the diffusion energy along or across the

steps. The actual situation is rather complicated since the final structure is defined from "very beginning of nucleation stage", as reported by Harald Brune [53] and references therein. It is reasonable, as the nanowires are well-separated from each other, the nucleation density is a constant since the beginning of nucleation as long as the experimental conditions are not varied during wire growth. Hence, the beginning stage of nucleation plays a major role in our case.

Further, Jałochowski and Bauer claimed that the average length of the nanowires depends inversely on the nucleation density, as reported in Ref [54].

The preceding investigation mentioned above can then be expressed in an universal equation that reflects the dependency of the length of the wires on the experimental conditions:

$$\frac{1}{\langle L \rangle} \sim n_x \sim \left(\frac{F}{\upsilon}\right)^{\frac{i}{i+2}} \exp \frac{E_i + iE_\mathrm{d}}{kT(i+2)}, \tag{4.2.7}$$

where F is the evaporation rate (or flux), υ vibration frequency of adatoms, and i the critical cluster size, E_i and E_d are binding energy of the critical cluster size and activation energy of the surface diffusion of adatoms, respectively.

It is not simple to isolate individually the variations as seen in equation 4.2.7 as they depend on each other. For instance, T also defines the activation energy E_d and the binding energy of the critical cluster size. The change in flux might lead also to a change in the critical cluster size.

Generally, taking into account also the dependency of the average length on the coverage, equation 4.2.7 reveals that the average length of the nanowires is defined further by three more experimental parameters: substrate temperature T, evaporation rate (flux) F and the substrate character itself (substrate in short form) which defines the activation energy at certain temperature condition.

As can be seen already in Figure 4.2.2, the nanowires are getting longer with increasing surface coverage. Figure 4.2.5 shows the role of three other parameters at the same coverage of 5 ML: substrate temperature, flux and substrate.

Figure 4.2.5(a) shows the role of T in the range from 270 K up to 320 K. Substrate used was Si(557), flux $F = 605 \pm 10$ s/ML. The average length $\langle L \rangle$ decreases with T within this range but a stronger absorption at resonance is observed, indicating that wires are getting shorter but more uniform in length. The matching of two experimental curves recorded at 297 K reveals

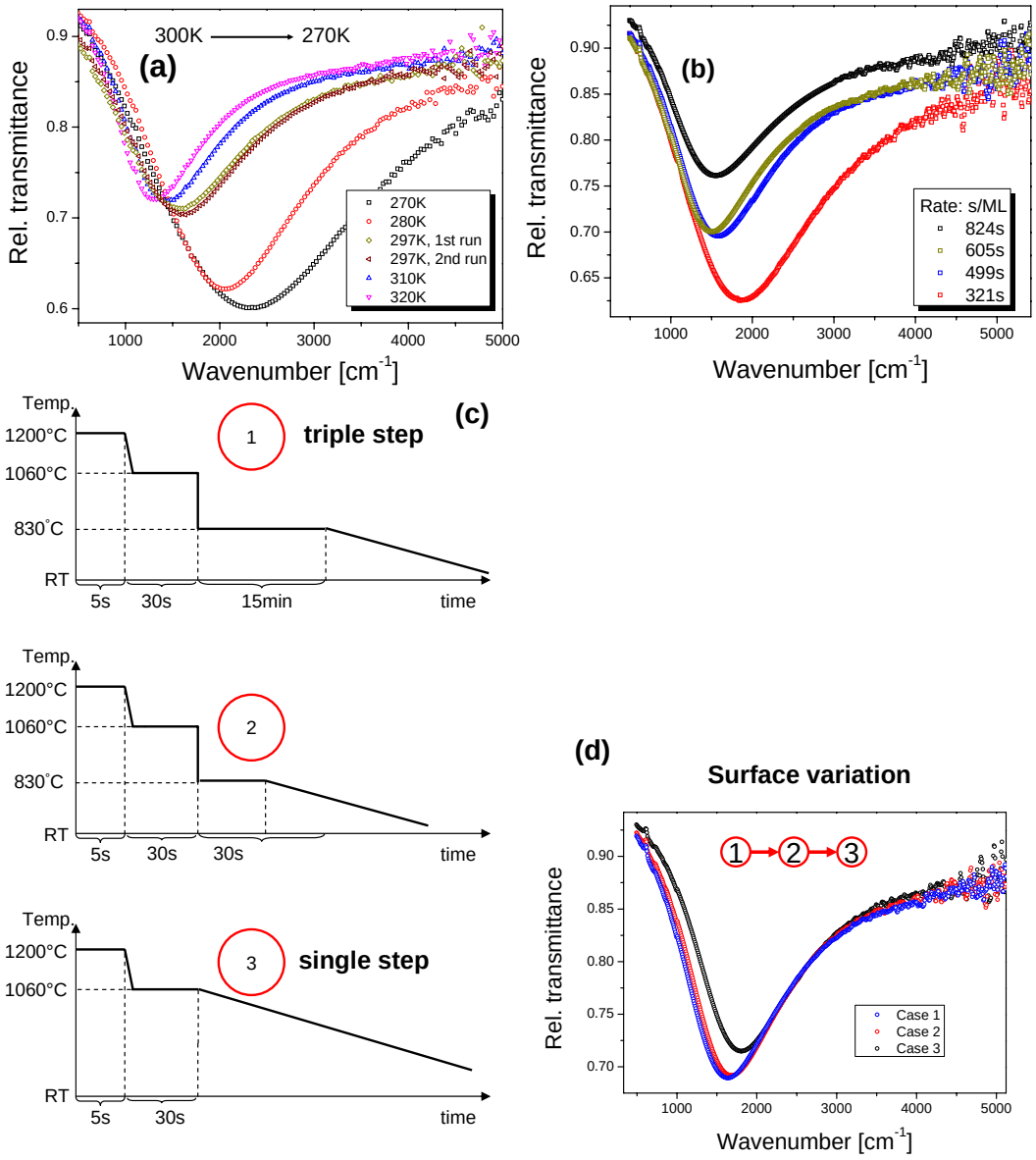

Figure 4.2.5.: Dependency of the plasmonic resonance position (reflects the average length) on the experimental conditions. The intention was to keep a constant coverage at 5 ML and vary other three parameters including substrate temperature, flux and surface reconstruction in figure (a), (b) and (c), respectively. Detail in the text.

the reproducibility of the experiments.

Figure 4.2.5(b) shows the role of flux. The substrate was Si(557) at a temperature $T = 297\,\mathrm{K}$. The higher rate leads to shorter wires but also stronger plasmonic absorption. Because of having the same coverage, stronger plasmonic absorption reveals that there is more nanowires at resonance contribute to the total absorption, meaning also that in this case, nanowires have better uniformity. Within the range from around 500 s/ML to 800 s/ML, there was no significant change observed. For a certain thickness, at RT, on Si(557) surface, one can easily tune the average length of wires to the value interesting for investigation. For instance, to avoid the influence of the vibration signal of water located from $1500\,\mathrm{cm}^{-1}$ to $1800\,\mathrm{cm}^{-1}$, one can increase the flux.

Figure 4.2.5(c) and (d) show the role of substrate Si(557). The crystallography does not change, but the surface reconstruction is modified by applying different experimental procedure. Chaika et al. [59, 60]reported on the variation of the step periodicity of Si(557) as partly indicated in 4.2.5(c). For a systematic investigation, only the annealing process at 830 °C is changed to form different reconstructions.

As reported by Chaika *et al.* [60]:

1. long annealing time at 830 °C (schema 1) produces triple step structures (stair-case like shape cross the steps).

2. short annealing at 830 °C (schema 2): there was no STM observation so far.

3. quenching from 1060 °C (schema 3) produces single step structures.

Figure 4.2.5(d) shows that schema 1 produces longer wires with better uniformity.

In summary, the tuning ability of average length of wires has been established. Four parameters have been found to control average length of the wires: coverage, surface temperature, flux and surface itself.

4.2.3. Shape relaxation

As mentioned in Chapter 2 and, especially studied by Venables and co-workers in 1984 [61], and Harald Brune later [53], the growth of metal nanoobjects in the self-organization process is a “non-equilibrium kinetic phenomena”. Therefore, when the material deposition stops, the nanostructures start to relax in shape to approach the equilibrium stage via mass transport by surface diffusion.

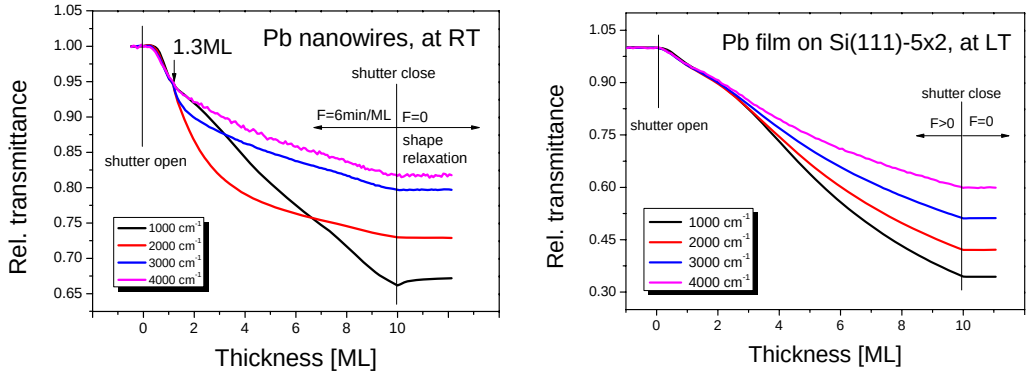

Figure 4.2.6.: A comparison of the IR relative transmittance spectra of two different samples: lead nanowires on vicinal and lead nanofilm on silicon flat surface which have been grown at different substrate temperature. For the case of nanowires, a polarizer is used, as explained in the text.

For the case of metal nanoparticles, there exists a plenty of research touching this problems. The obtained result so far is mainly based either on simulations [62] or scanning tunneling microscopy (STM) with real time observations [63].

This short section intends to report on the real-time spectroscopic observation of the mass transport occurring at the tip ends of the as synthesized nanowires that leads to the shorter wires but better crystallity. The observed experiment has been performed under the parallel excitation regime of electric field to the long axis of the nanowires. Because of having a high aspect ratio between length and width, it is expected that the relaxation is taking place mainly at the tip-ends of the wires.

Figure 4.2.6 shows a comparison of the IRS relative transmittance (TR) of lead nanowires and lead nanofilm, with the same coverage 10 ML for each sample. The lead nanowires were synthesized on the bare Si(557) surface at RT and the lead film was grown on the Au/Si(111)-5×2 surface which had been cooled down with liquid nitrogen.[8] The IR spectrum of the film shows the decrease of the transmittance at lower frequency, indicating the conventional Drude behavior of a metal film. When the evaporation stops at 10 ML, marked by the arrow, the relative transmittance stays at constant with time. The time duration for recording this spectrum was about 8 minutes.

In contrary to that, the IR spectrum of the nanowires shows different

[8] Au/Si(111)-5×2 is formed by using the standard sample preparation as explained in Chapter 3, 0.65 ML of gold was deposited onto Si(111) surface. A RHEED pattern of Au/Si(111)-5×2 can be found in Appendix A.

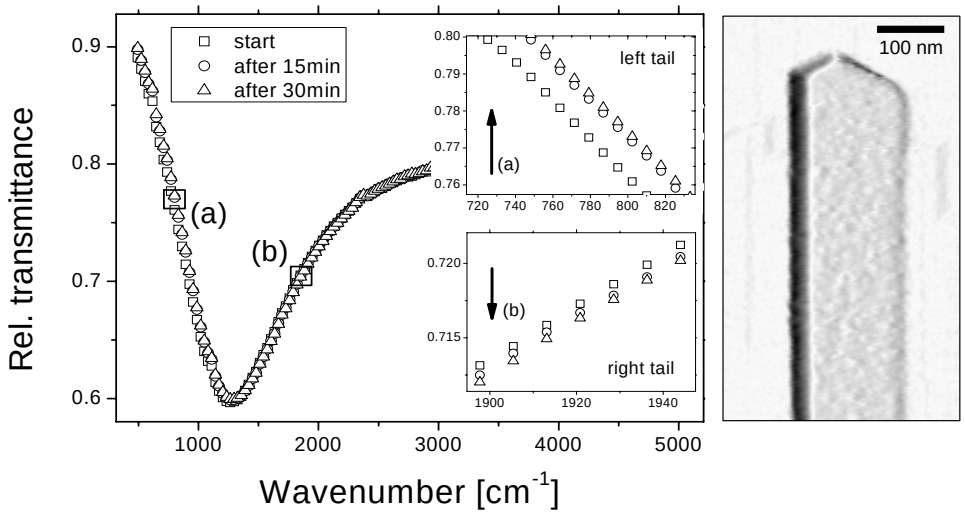

Figure 4.2.7.: The time evolution of change of the IR spectra of as-synthesized nanowires right after closing shutter, after 15 min and after 30 min are shown. The zoom-in positions are marked as (a) and (b) in the main figure and are replotted in the insets. A typical AFM image of the tip end of a Pb nanowire, 3 ML of coverage, taken *ex-situ* in contact mode.

tendency right after closing the shutter. We observed the increase of the transmittance at frequency 1000 $cm^{-1}$and a slight decrease at resonance 2000 cm^{-1}. The corresponding resonance curve of these nanowires is shown in Figure 4.2.7 indicating that the resonance frequency ω_{res} lies at about 1300 cm^{-1}. This change reveals the fact that the transmittance of the left tail of the resonance curve increases while in the meantime, the right tail decreases the transmittance.

Having a closer look at Figure 4.2.7, one can zoom in into the tails and confirm the relative movement of the resonance curve after 30 min leads to higher frequencies, meaning that the nanowires are getting shorter and the relative transmittance at resonance also increases.

In order to schematically explain the shape relaxation effect, a growth model offered by Li and co-workers is highly possible to be considered [64]. In this model, the role of diffusion around the corner islands so-called anisotropic corner rounding diffusion (ACR) plays a major role in the formation of the elongated islands on the step surfaces.

Figure 4.2.8 shows a schematic illustration of the possible diffusion processes on the metal (110) surface with the notation for the activation energy [64]. According to Li and co-workers, the black balls denote the adatoms on the

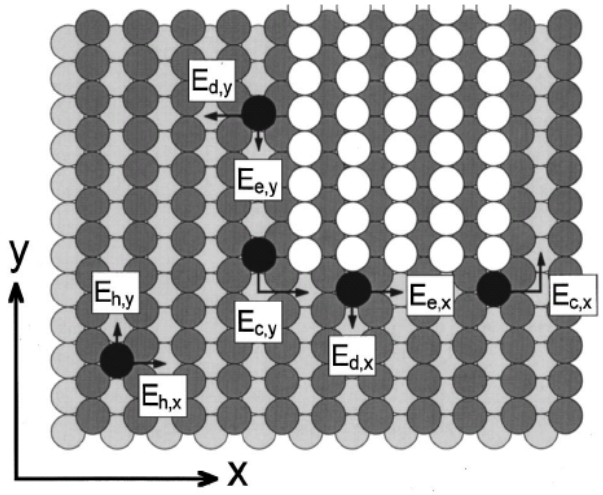

Figure 4.2.8.: Model to explain the shape relaxation by Li *et al.* [64]

surface and the possible movements of them are expressed as corresponding activation energy.

1. Terrace diffusion notated by $E_{\mathrm{h,x}}$ and $E_{\mathrm{h,y}}$, herewith the $E_{\mathrm{h,y}} < E_{\mathrm{h,x}}$ as the y direction is an easy axis for diffusion.

2. Edge diffusion's by $E_{\mathrm{e,y}}$ along the long edge and $E_{\mathrm{e,x}}$ along the short edge, respectively.

3. Two-step movements of adatoms around the corners of the edges, which are notated by the effective corner diffusion $E_{\mathrm{c,y}}$ and $E_{\mathrm{c,x}}$ accordingly from y to x and vice-versa.

4. Detachment movement of adatoms from the edge, denoted by $E_{\mathrm{d,x(y)}}$.

According to this model, nanowires are developing in length as the diffusion along the steps (edge diffusion) bring the adatoms to the corners and the diffusion from y to x around the corners are more dominant than the other directions. Subsequently, when the nucleation stops, these diffusion processes are suddenly stopping, while in the meantime the others are still in kinetic. The diffusion from x to y turns out to be more stronger, leading to the shortening of the nanowires.

In conclusion, the observation of the shape relaxation is reported, followed by the shortening of the wires. The corner rounding diffusion based ACR model is a plausible candidate to explain this effect by taking into account the mass transport of the lead adatoms at the tip-ends of the nanowires.

4.3. Temperature related enhancement of plasmonic absorption

The intention of this part is to show a systematic experiment on the enhancement of plasmonic absorption at low temperature and at various coverages. It is found out that the absorption signal at the resonance frequency increases when the temperature is decreased. There was no observation of a shift of the resonance frequency due to temperature changes. In fact, there is a small change in the refractive index of the silicon substrate. The reason for this enhancement is attributed mainly to the reduction of electron-phonon scattering which is carefully explained with help of the Debye model in solid states. Other scattering events such as electron-electron scattering, electron-surface scattering and radiative damping are proven to be temperature-independent. Additionally, the contribution of electron-surface scattering is taken into account to describe the role of the film thickness on the reduction of electron scattering.

4.3.1. Experimental data

As already mentioned in Chapter 3, in order to measure the lead nanowires at low temperature, the sample has to be homogeneous in a huge area since the entire sample will be laterally shifted due to cooling. Before carrying out the cooling experiments, IR relative transmittance measurements were recorded to show the deviation of the minimum transmittance to be smaller than 0.1 % in entire the spatial shift of sample position (about 1.5 mm if cooling with LHe). Also, in such large area, there was no shift of the resonance frequencies.

The temperature-dependent measurements are conducted in-situ, therefore the precision of the temperature measurement has to be fulfilled in the entire process. A good agreement has been found during warming up from LHe rather than during cooling down from RT, because the temperature gradient is smaller for the former case (see Figure 3.1.2). Importantly, several test runs were performed and showed there was no morphological distortion at the lowest temperature (~ 25 K) in comparison to the RT one. As described in section 3.5.2, all of the data for the LT experiments of lead nanowires was performed during warming up from LHe temperature.

Figure 4.3.1 shows behavior of the relative transmittance for an ensemble as well as the extinction cross section of a single nanowire of the 3 ML of lead coverage beyond heating from 25 K to around 280 K. The enhancement of plasmonic absorption is clearly identified. The absorption strength was

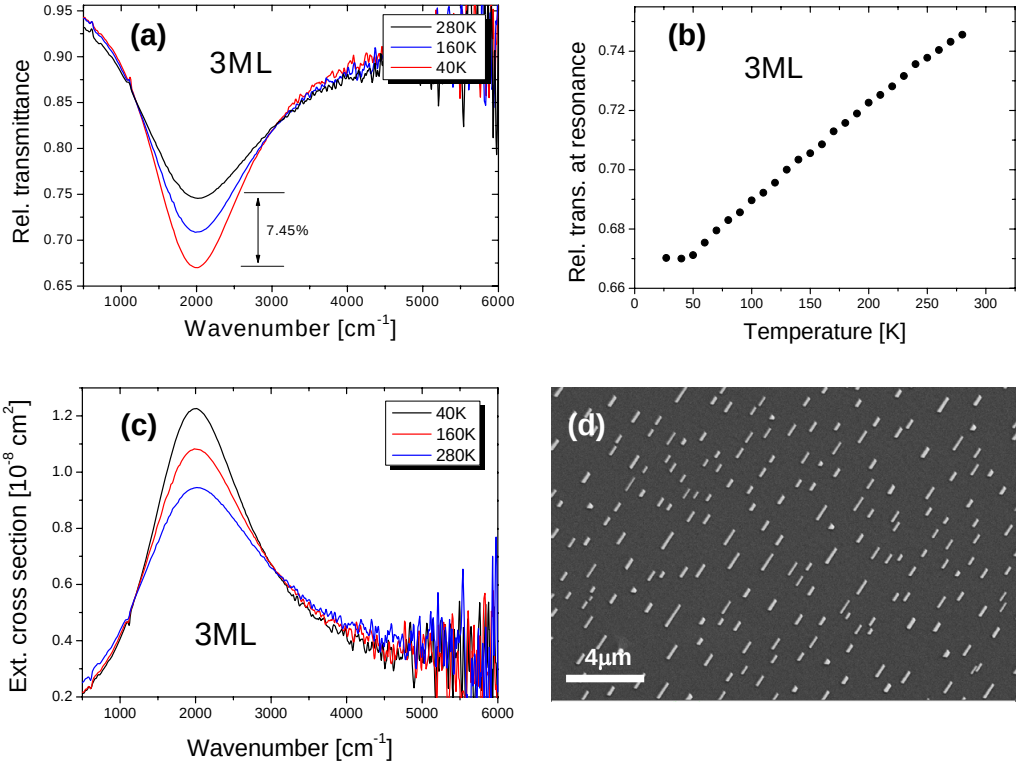

Figure 4.3.1.: A typical temperature-dependent behavior found for the lead nanowires, this is an example for 3 ML of coverage. Figure (a): the evolution of the relative transmittance spectra of 3 ML of Pb nanowires versus temperature. Figure (b): The plot of minimum transmittance of spectra in the left versus temperature.. Figure (c): The plot of the extinction cross section of single nanowire. Figure (d): the corresponding scanning electron microscopy image of this sample, showing that nanowire density is $5.95 \times 10^{-7}\,\mathrm{cm}^{-2}$, image was taken 4 days after being removed from UHV. SEM picture is by courtesy of Daniel Weber, KIP.

increased by 7.45 % in the entire cooling range from RT to LHe, followed by the increase of the extinction cross section of single nanowire.

Looking at Figure 4.3.1 (b), a monotonic decrease of the relative transmittance was obtained from RT down to around 50 K, indicating a linear dependency of the absorption enhancement versus temperature. A reverse tendency is easily to be inferred for the extinction cross section since it is related to the relative transmittance and the nanowire density N as explained in Chapter 2:$\sigma_{\text{ext}} = (1 - T_{\text{rel}})(n_{\text{Si}} + 1)/2N$.

Also, the resonance frequencies of the spectra were not shifted at low temperature. Instead, there is a small change of the refractive index of the surrounding media which partly defines the resonance frequency of the optical antenna [22]. In contrary to this work, Liu *et al.* reported a shift of the resonance frequencies when measuring on gold bipyramids on quartz substrate [65].

Theoretically, if there is any shift of the resonance frequency at low temperature, it must be related to either the refractive index of the surrounding media or the plasma frequency of the metal used 4.2.1. Herewith a brief estimation for a possible shift due to the change of refractive index is brought out for discussion.

B. J. Frey *et al.* [66] reported that the value of the refractive index of silicon at 2000 cm^{-1} is 3.39 and 3.42 at 30 K and 295 K, respectively. Since the length of a macroscopic wire does not change by cooling to low temperature, one can use the optical antenna theory (equation 4.2.3) to estimate a variation in the resonance frequency of about 16 cm^{-1} to higher energy. Surprisingly, within this work, there was no shift of resonance frequencies obtained so far.

In order to get an insight into the origin of the drastic enhancement of plasmonic absorption, a finite-different time domain (FDTD) calculation has been performed on a single rectangular cross section lead nanowire which has a length of 600 nm, and a height of 60 nm. The result is shown in Figure 4.3.2. By varying the scattering rate of the lead material used in the nanowire from the bulk value to smaller ones, we observed also a decrease of relative transmittance. Importantly, also there was no frequency shift obtained.

Upon the similar tendency between the experimental results and the calculation one reveals that the origin of the enhancement of the plasmonic absorption at low temperature is related to the reduction of the scattering rate, which is specific for the electron scattering in metal.

To get further understanding of the dependency of enhancement behavior, a series of samples with various thicknesses has been synthesized and examined. Figure 4.3.3 shows the data of nanowires at different coverage, from 2 ML to 10 ML. Figure (a) shows four samples retrieved in four different runs with

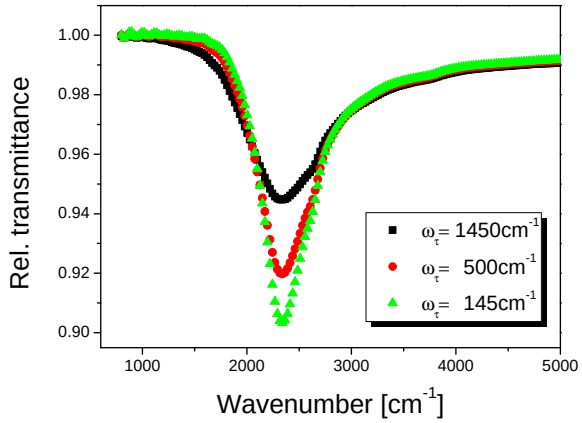

Figure 4.3.2.: Finite-different time domain calculation of a single Pb nanowire on silicon substrate, performed for three different scattering rates, ranging from bulk value 1450 cm^{-1} to smaller ones. Calculation by F. Neubrech.

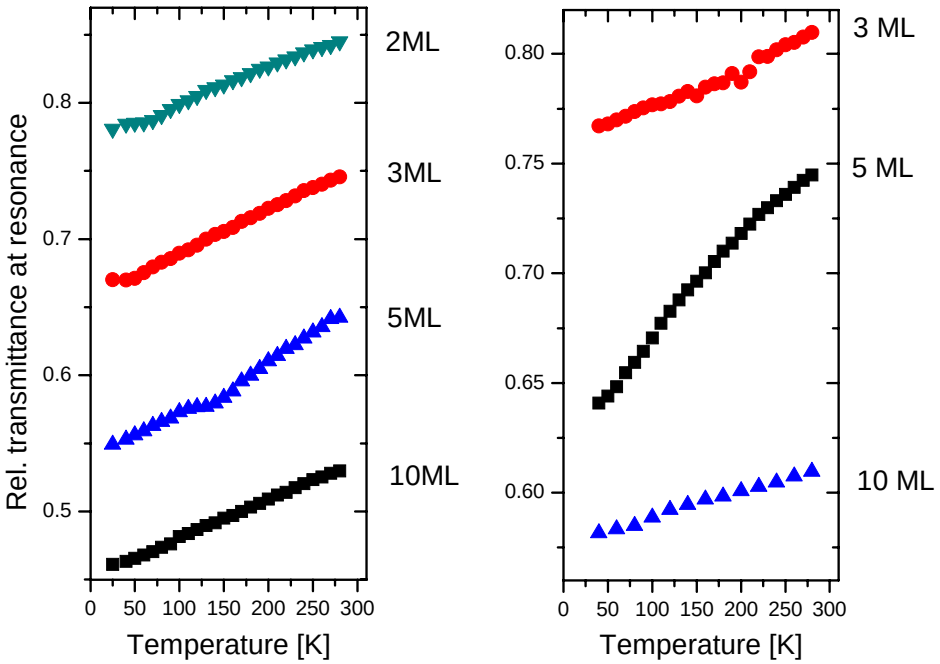

Figure 4.3.3.: The dependency of the plasmonic enhancement on temperature and thickness of the lead wires. Figure (a): developement of the minimum relative transmission of the nanowire resonance with temperature for four different samples (different runs) with similar experimental conditions. Figure (b): Three other samples with similar condition in surface, substrate temperature and thickness, in comparison to Figure (a); but different in evaporation rate.

nearly the same experimental conditions: the substrate was Si(557), lead was deposited on the surface kept at RT, and the flux was about 6 min per monolayer. It shows the same tendency of the decrease of relative transmittance versus temperature. In contrary to that, Figure (b) shows three other runs where the flux has been changed in the way that the flux for 3 ML and 10 ML was about 8 minutes per monolayer, which is smaller than the case for 5 ML of around 4.5 minutes per monolayer.

Figure 4.3.3 indicates strongly that at the same experimental condition which is proven to give the same nucleation density, the dependency of the plasmonic enhancement at low temperature does not depend on the thickness of the nanowires.

4.3.2. Theoretical explanation

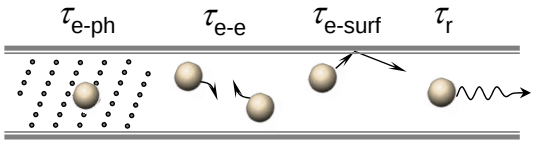

Figure 4.3.4.: Schematic representation of different types of electron scattering in metal: electron-electron, electron-phonon and electron-surface scattering.

The total relaxation rate for conduction electrons in solids $1/\tau_{\text{bulk}}$ is given by

$$\frac{1}{\tau_{\text{bulk}}} = \frac{1}{\tau_{\text{e-ph}}} + \frac{1}{\tau_{\text{e-e}}} + \frac{1}{\tau_{\text{e-surf}}} + \frac{1}{\tau_{\text{r}}}, \tag{4.3.1}$$

where $1/\tau_{\text{e-ph}}$ reflects the electron-phonon, $1/\tau_{\text{e-e}}$ the electron-electron, $1/\tau_{\text{e-surf}}$ the electron-surface and $1/\tau_{\text{r}}$ the radiative relaxation rate. Details of electron scattering have been analyzed in Ref [65] for the case of gold bipyramid structures in the visible range. Within this work the scattering mechanism in nanowires in the infrared will be established. Details of the scattering events are explained below.

Electron-electron scattering Lawrence and Wilkins reported on the electron-electron scattering in the following expression [67]:

$$\frac{1}{\tau_{\text{e-e}}} = \frac{\pi^3 \Sigma \Delta}{12 \hbar E_{\text{F}}} \left[(k_{\text{B}} T)^2 + \left(\frac{\hbar \omega}{2\pi} \right)^2 \right], \tag{4.3.2}$$

where Σ is the Fermi-surface average of scattering probability and Δ is the fractional umklapp scattering. It is assumed that the scattering probability and the umklapp scatterings of electrons are constants. There is one important issue that electron-electron scattering depends on temperature and infrared photon energy, as can be seen from equation 4.3.2.

Within this experiment, the infrared photon energy covers a range from 124 meV to 1240 meV with frequency ranging from 1000 cm^{-1} to 10.000 cm^{-1}, respectively. The thermal energy $k_B T$ at RT is 25 meV and at 30 K is 3.44 meV. One can make a comparison for a frequency of 1000 cm^{-1}: at RT, the photon energy is one order of magnitude higher than thermal energy. The difference becomes even larger at LT where the photon energy is two orders of magnitude higher than thermal energy. Therefore, the dependency of electron-electron scattering on temperature can be neglected.

Electron-phonon scattering Electron-phonon scattering was treated by Holstein in Ref [68] by considering the conduction electrons as free electron gas. The phonons are described by the Debye model. As it is explained in Chapter 2 and Ref [58], there is no interband transition taking place in our measurement range, therefore the dependency of electron-phonon scattering on temperature is expressed as follows:

$$\frac{1}{\tau_{\text{e-ph}}} = \frac{1}{\tau_0}\left[\frac{2}{5} + 4\left(\frac{T}{\Theta_D}\right)^5 \int_0^{\Theta_D/T} \frac{z^4}{e^z - 1} dz\right], \tag{4.3.3}$$

where τ_0 is a constant for a given metal and Θ_D is the Debye temperature of the material used.

In order to derive τ_0 for the case of lead, one has to start from bulk material in which the other scattering events can be neglected except electron-phonon scattering. The electron scattering rate in the bulk material is $\omega_\tau = 1450 cm^{-1}$ [69]. Scattering time τ_0 therefore is $\tau_0 = 12.75$ fs. The Debye temperature of lead is 88 K [70].

Electron-surface scattering As mentioned in section 4.2, the lead nanowires have triangular cross section and at 10 ML of lead coverage, for certain experimental conditions, the average height of lead nanowires is about 32 nm. The electron mean free path in bulk lead is:

$$l_P = v_F \tau_0 \tag{4.3.4}$$

with the Fermi velocity $\upsilon_{\mathrm{F}} = 1.83 \times 10^6\,\mathrm{m/s}$ [24], $\tau_0 = 12.75\,\mathrm{fs}$. The electron mean free path turns out to be about 23 nm, comparable to the average height of the wires at 10 ML coverage. It is worth from here to take into account the electron surface scattering. In case of nanowires, it is well-treated by the Dingle model [71]:

$$\frac{1}{\tau_{\text{e-surf}}} = \frac{1-p}{1+p}\frac{\upsilon_{\mathrm{F}}}{d}, \tag{4.3.5}$$

where υ_{F} is the Fermi velocity of electrons in lead, $1-p$ is a non-specular portion of electron surface scattering and d is the average diameter of the nanowire. From equation 4.3.5, it can be seen that at a certain thickness, the Fermi velocity which is a characteristic of the used material, causes the difference in electron-surface scattering for different materials. However, as reported by Jałochowski and Bauer [5], lead nanowires fabricated by this method are single crystalline, thus it is reasonable to assume that $p \approx 1$, meaning that we have an absolute contribution of specular scattering, the electron wave function is in-phase before and after the scattering event (see general mechanisms in Figure 4.3.4). Equation 4.3.5 reveals that electron-surface scattering is thickness-dependent but temperature-independent, and it is rather small for the case of single crystalline wire.

Radiative scattering For the case of plasmonic absorption of the nanoantenna, the conduction electrons that contribute to the surface plasmon are moving coherently under an excitation of an external electric field that is parallel to the wires. The electromagnetic field therefore can simultaneously be emitted by the conduction electrons, leading to a decrease of the plasmon energy. The radiative emission of free electrons might be considered as a radiative scattering, as reported schematically by C. Sönnichsen *et al.* for the case of metal nanoparticles [72].

In fact, the contribution of radiative damping is only about 1.5 % in the total damping in the case of metal nanoparticles, as reported by U. Kreibig and Vollmer [73]. The measured radiative damping of the nanorods with aspect ratio of 3:1 is by far smaller than that of nanoparticles due to smaller volume in the visible range[72]. Below, an approximation of radiative damping for the case of lead nanowires will be presented.

Theoretically, M. Liu *et al.* [65] reported radiative damping in the following

expression:

$$\frac{1}{\tau_{\mathrm{R}}} = \frac{2\,\omega^2\,e^2\,\sqrt{\varepsilon_{\mathrm{m}}}\,N}{3\,m\,c^3}, \tag{4.3.6}$$

where ε_{m} is the dielectric constant of the surrounding media, N the total number of free electrons in the wire, m the electron mass and c is the velocity of light. Equation (4.3.6) reveals that this damping term depends on the frequency of the electric field and on the number of free electrons contributing to the surface plasmon, but not on the temperature.

In this work, the dielectric constant of surrounding media can be assumed as :

$$\varepsilon_{\mathrm{m}} = \frac{1}{2}\left(\varepsilon_{\infty} + \varepsilon_{\mathrm{S}}\right). \tag{4.3.7}$$

The total number of conduction electrons in one lead nanowire is derived by taking into account the conversion of the shape of the wires from a triangular cross section into a circular cross section. The number of free electrons that contribute to the surface plasmon of such cylindrical wires then can be expressed as:

$$N = 4\frac{\pi\,\langle R\rangle^2\,\langle L\rangle}{M_{\mathrm{Pb}}}\rho\,N_{\mathrm{A}}, \tag{4.3.8}$$

where $\langle R\rangle$ and $\langle L\rangle$ are the average radius and length of the nanowires, respectively, $\rho = 11.34\,\mathrm{g/cm^3}$ is the mass density of lead, $M_{\mathrm{Pb}} = 207.2\,\mathrm{g/mol}$ is the mass per mol, $N_{\mathrm{A}} = 6.02 \times 10^{23}\,\mathrm{mol^{-1}}$ is the Avogadro constant. The number 4 represents the fact that every Pb atom contributes 4 electrons into the surface plasmon of wires.

In order to calculate electron-surface and radiative scattering, systematic series of samples have been fabricated. As mentioned in section 4.2.2, the average length of the nanowires can be tuned precisely by controlling four experimental parameters: evaporation time and rate, substrate temperature and substrate diffusion energy. By doing so, the nucleation density is kept constant from the beginning stage of nucleation, therefore the average length of the wires is reproducible.

Figure 4.3.5 shows plasmonic absorption spectra of different nanowires with different coverages, from 2 ML to 10 ML. The four experimental parameters were kept constant throughout sample preparation.

AFM studies were also done for the case of the 3 ML sample, showing that

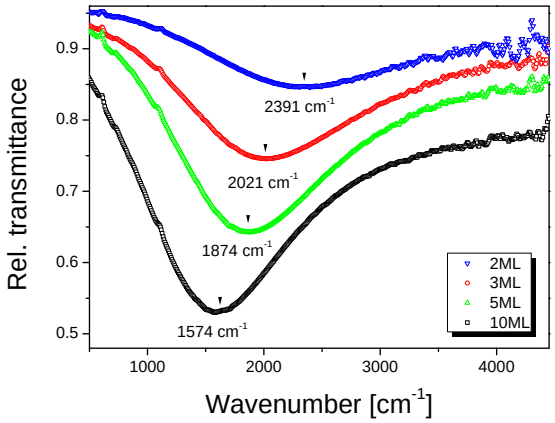

Figure 4.3.5.: IRS of series of samples synthesized under the same experimental conditions, but different coverages, ranging from 2 ML to 10 ML. Spectra were taken at RT, electric field parallel to the wires. Experimental parameters are as described to Figure 4.3.5.

the average diameter of the wires is about 15.22 nm. The average diameter for the case of 10 ML is roughly taken from the sample shown in section 4.2 of about 33.5 nm. From that starting point, the average diameters for 2 ML and 5 ML are derived with the assumption of a linear dependency of average radius with coverage.

By using data from IRS and AFM measurements, it is possible now to use the optical antenna theorem offered by L. Novotny [22] to calculate the average length of the nanowires. Data is shown in table 4.1. Also, number of free electrons in an individual nanowire is calculated based on Equation 4.3.8. Electron-surface scattering is calculated for the case of $p = 0$ - assumption of no specular scattering at the surface which is probably not the case, see above. Radiative damping at frequency of 1000 cm^{-1} is estimated and listed in table 4.1 as well.

4.3.3. Plasmon linewidth of the nanowires at low temperature

In the publication in 2006, F. Wang and R. Shen reported theoretically on the general properties of local plasmon in the nanostructures [74]. According to their theory, the electron scattering (scattering rate) in the structure which causes the damping of plasmon energy is simply determined by the spectral linewidth of the plasmon resonance.

Figure 4.3.6 shows the normalization of the plasmon resonance in the case

Table 4.1.: Electron-surface and radiative scattering are calculated from equations 4.3.5 and 4.3.6 for various thicknesses, ranging from 2 ML to 10 ML. The average diameter of the wires was determined from AFM experiments for two cases: 3 ML and 10 ML, the other values are derived by a linear assumption of average radius with coverage.

Thickness [ML]	$\langle R \rangle$[nm]	$\langle L \rangle$[nm]	N [10^7]	$\omega_{\text{e-surf}}$[meV]	ω_{r}[meV]
2	12.6	276	2.43	52.0	1.28
3	15.22	428	5.49	47.8	2.90
5	20.4	639	14.7	39.5	7.79
10	33.5	1324	82.4	18.0	43.5

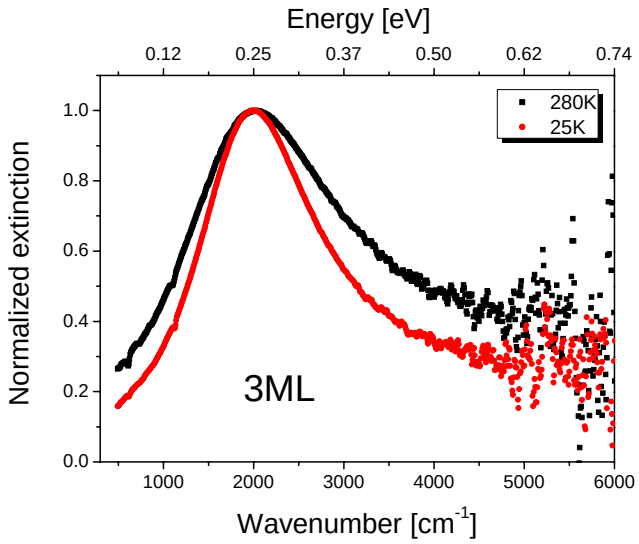

Figure 4.3.6.: Normalization of the extinction cross section to find out the linewidth FWHM of the spectral shape. Data is shown for the case of 3 ML of coverage at two different temperature: 25 K and 280 K.

of 3 ML nanowire, at 25 K and 280 K. There is a clear evidence that FWHM is decreased at low temperature, indicating also the reduction of plasmon damping.

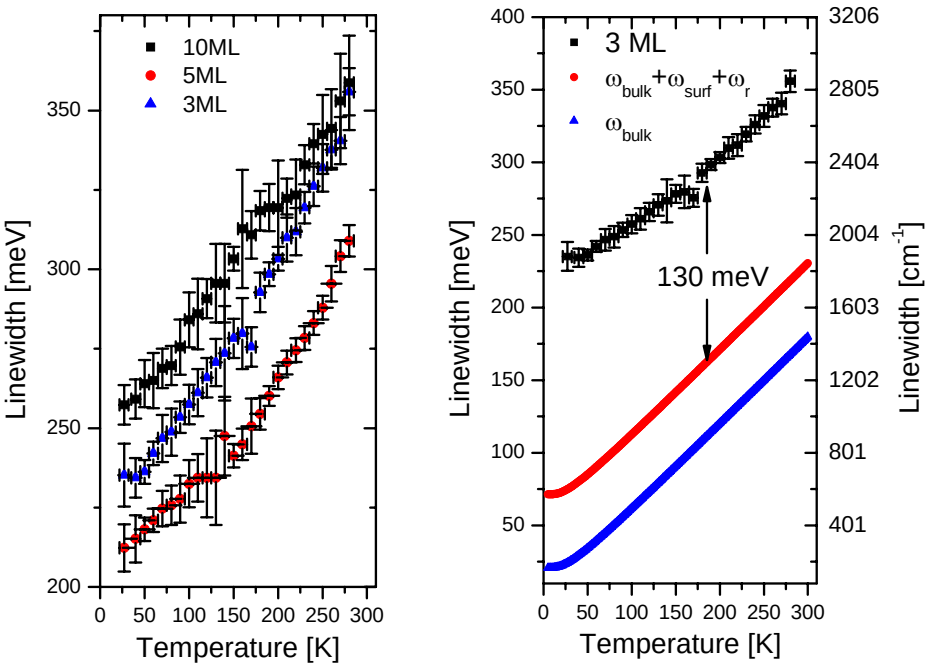

Figure 4.3.7.: Experimental and calculation result of the electron scattering in lead nanowire versus temperature. Left: the FWHM of the plasmon linewidth of different thickness is plotted versus temperature. Right: a comparison of experimental data of 3 ML wire and calculation data. The blue curve is for bulk material, which takes into account only electron-phonon scattering. The red curve takes into account additionally two scattering terms: electron-surface scattering and radiative relaxation, as estimated from Table 4.1.

Figure 4.3.7 shows a comparison between experimental data of FWHM and calculation of electron scattering in lead nanowire with different thickness.

The left image of Figure 4.3.7 shows an offset due to the thickness variation. An offset of about 50 meV is clearly determined. In general, the nanowires show the same tendency of the FWHM with temperature. A reduction of plasmon linewidth of about 27.7 % from 280 K to 25 K is clearly observed.

The right image shows a comparison between experimental FWHM and calculation data. The comparison is considered for the case of 3 ML since it has a better support (more precise) by the corresponding SEM picture, as shown in Figure 4.3.1. In case of taking into account bulk plasmon, radiative

damping and maximum of electron-surface scattering, an offset of about 130 eV indicates the discrepancy between theoretical prediction and experimental data. This offset can be attributed to temperature-independent terms of electron scattering in the nanowire and the broadening of the linewidth due to the length distribution over measured area.

In summary, a systematic work shown in the case of 3 ML coverage shows the enhancement of plasmonic absorption at resonance of nanoantenna at low temperature, accompanying by the increase of the extinction cross section in the single wire. The FWHM of the longitudinal mode (excitation parallel to the wires) follows a similar tendency with minimum of the relative transmittance versus temperature. The theoretical calculation also determines the agreement with the experimental data in that sense, but a discrepancy is found. It reveals to contribution of other temperature-independent terms to the total scattering.

4.4. Indium atom-chains

This chapter presents the results on the indium atom chains on silicon vicinal surfaces. In comparison to the Si(557) substrate, a Si(111) vicinal surface (Si(111)-vic from now on) provides wider terraces. In practice, such a surface can be considered as the imperfect domains of Si(111) with full-reconstructed surface made of the 7×7 superstructures.

Si(111)-vic is produced by cutting the silicon crystal with an inclined angle of 1° from [111] towards [$\bar{1}\bar{1}2$] direction. In this experiment, the wafers had similar characteristics as the Si(557) used for Pb nanowires.

The In-induced 4×1 (In4×1 from now on) is a superstructure made of indium reconstruction, supported by the silicon substrate. The 4×1 unit cell is defined with the consideration to the unit cell of the silicon underneath as the reference. Along the chain direction, the unit cell is (×1), it is as large as the unit cell of the silicon layers underneath. In the interchain direction, its unit cell is four time (×4) larger than the unit cell of silicon .

The fabrication approach of In4 × 1 was presented in the experimental part. Basically it consisted of the standard cleaning process, including *ex-situ* treatment with the chemical solvents and the flashing procedure performed in the UHV. Indium was evaporated from an alumina crucible onto the substrate that was kept at 3Indium atom-chains

This chapter presents the results on indium atom chains on silicon vicinal surfaces. In comparison to the Si(557) substrate, a Si(111) vicinal surface (Si(111)-vic from now on) provides wider terraces.

Si(111)-vic is produced by cutting the silicon crystal with an inclined angle of 1° from [111] towards [$\bar{1}\bar{1}2$] direction. In this experiment, the wafers had similar characteristics as the Si(557) substrate used for Pb nanowires.

The In-induced 4×1 (In4×1 from now on) structure is a superstructure made of an indium reconstruction supported by the silicon substrate. The 4×1 unit cell is defined with the consideration to the unit cell of the silicon underneath as the reference. Along the chain direction, the unit cell is as large as the unit cell (×1) of the silicon layers underneath. In the interchain direction, its unit cell is four times (×4) larger than the unit cell of silicon .

The fabrication approach of In4 × 1 was presented in the experimental part. Basically it consisted of the standard cleaning process, including *ex-situ* treatment with the chemical solvents and the flashing procedure performed in UHV. Indium was evaporated from an alumina crucible onto the substrate that was kept at 350° C. Similar to the case of the gold atom chains, In atom chains were produced on the surface by self-assembly. The surface was then subsequently cooled down to RT for the spectroscopic investigations.

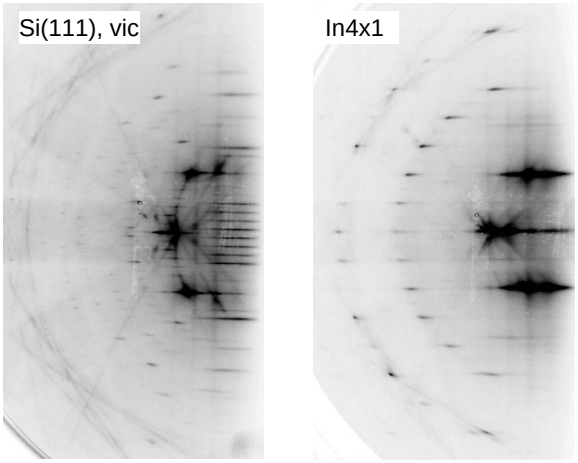

Figure 4.4.1.: RHEED diffraction patterns of the Si(111)-vic substrate and In-induced 4×1 reconstruction on the surface. Electron energy 20 keV, electron incident angle 1∼2°. The electron beam was directed perpendicular to the atom chains.

Figure 4.4.1 presents the electron diffraction patterns of the cleaned Si(111)-vic surface and In4×1. In comparison to the Si(111) flat surface whose RHEED pattern was shown in the previous chapter 3, the Si(111)-vic surface showed elongated diffraction streaks instead of spots of the 7×7 reconstruction. The reason for that is that the Si(111)-vic surface has a small offcut angle of about 1°, therefore the domain size of 7×7 was smaller producing the elongated streaks. In principle, such a streak can be utilized to determine the terrace width of the step-induced structures on the silicon surface.

The RHEED pattern of the In4×1 is shown on the right of figure 4.4.1. The 7×7 reconstruction of the surface was no more present but some new diffracted spots have arisen. The ×1 reconstruction was oriented in the interchain direction, while in the chain direction ×4 was obtained. It is worth to notice that the ×4 looks like ×2 reconstruction, but without an additional spot in between ×1 of the fundamental ones.

4.4.1. Electronic structure of In4×1

Figure 4.4.2 presents the atomic structure of In4×1 with an indication of the unit cell. It is shown in this figure that In4×1 is not an "ideal" atomic chain as it is composed of two zig-zac indium chains on each ensemble.

The band structure calculation which is presented in figure 4.4.2 shows the electronic structure of the In4×1 in two different directions: $\bar{\Gamma}\bar{X}$ - the

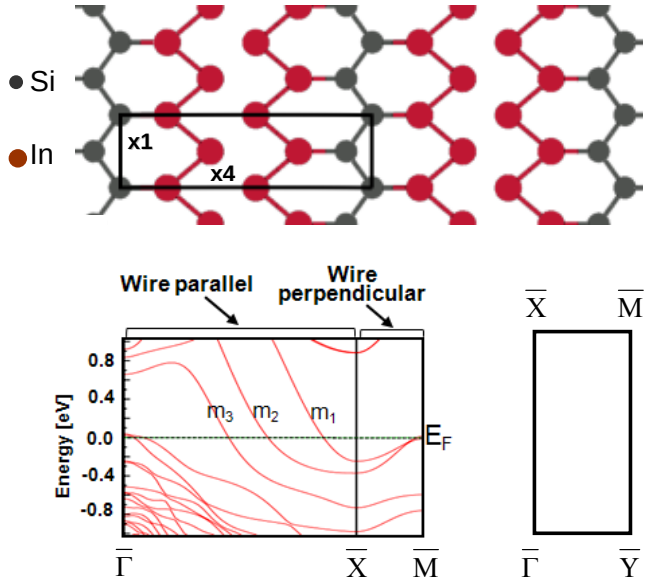

Figure 4.4.2.: A simulated indium reconstruction on the Si(111)-vic surface. Above: the atomic structure of In4×1 with the unit cell indicated. Below: a band structure calculation for both directions: wire parallel and wire perpendicular directions. The first Brillouin zone is indicated (not scaled). Reproduced from [75].

chain direction; and $\bar{X}\bar{M}$ - the interchain direction. As can be seen in this calculation, in the $\bar{\Gamma}\bar{X}$ direction (along the chains), there are three electron bands labeled m_1 m_2 and m_3 crossing the Fermi level producing the metallicity along the chain. In contrary to that, in the interchain direction, two electronic levels slightly touch the Fermi level. Theoretically, the metallicity can be found only along the chains.

In practice, Kanagawa *et al.* [50] reported a strong anisotropy of the conductivity by direct contact measurements (four-point probe approach). Their finding shows that the conductivity in the indium chain is 60 times higher than in the interchain direction. As can be inferred from that, the electrons are more free in the chains, and they have the electron mean free path of about 6 nm.

From that point of view, it is worth to consider the Drude model which serves as guidance for interpretation of the origin in the anisotropy of metallic conductivity. According to the Drude theory, we are going to take into account the plasma frequency of electrons ω_P and the electron relaxation rate ω_τ as two parameters. The optical conductivity of the metal can be described

as:

$$\sigma_{\text{opt}} = \frac{\omega_{\text{P}}^2}{4\pi\omega_\tau}\,, \tag{4.4.1}$$

where the plasma frequency is defined as:

$$\omega_{\text{P}} = \sqrt{\frac{ne^2}{\epsilon_0 m^*}}\,, \tag{4.4.2}$$

where n is the free electron density, e the electronic charge, m^* effective mass of an electron, ϵ_0 the vacuum permittivity.

To my knowledge, there were no experimental data about the plasma frequency published so far. In the theoretical work on the optical properties of the indium chains, X. López-Lozano *et al.* [76] defined the characteristic oscillator strength as:

$$S = L_{\text{slab}}\,\hbar^2\,\omega_{\text{P}}^2\,, \tag{4.4.3}$$

where L_{slab} is the thickness of 12 atomic layers and the vacuum region with the same extent. The characteristic strength in the chain direction is: $119.92\,\text{eV}^2\text{Å}$ and in the interchain direction is $24.09\,\text{eV}^2\text{Å}$. From this theoretical work, one can withdraw that the plasma frequencies in their calculations are: $\omega_{\text{P}_\parallel} = 48420\,\text{cm}^{-1}$ and $\omega_{\text{P}_\perp} = 21705\,\text{cm}^{-1}$ in the chain direction and in the interchain directions, respectively. The plasma frequency of the bulk material is: $\omega_{\text{P}} = 91880\,\text{cm}^{-1}$, as inferred from [77], and that the electron relaxation rate in the chains is $6410\,\text{cm}^{-1}$, inferred from [50].

From the expression in equation (4.4.2) and the plasma frequency values achieved above, it is possible to determine that the electron density n in the chain direction is five times higher than in the interchain direction. Further more, it is clear that the optical conductivity in the indium chain is much higher than in the interchain direction.

In order to understand in more detail the electronic transport occurring inside the indium chains, the information length of the electrons is defined as the distance that electrons can move within one circle of the electrical field. In the case of the AC conductivity experiment, the information length is frequency-dependent and is expressed as:

$$l_{\text{i}} = \upsilon_{\text{F}}\frac{2\pi}{\omega}\,, \tag{4.4.4}$$

where $\upsilon_{\text{F}} = \hbar k_{\text{F}}/m^*$ is the Fermi velocity of the electrons at the Fermi surface,

Table 4.2.: Characteristic parameters of the three electronic bands in the In chains direction, calculated at frequency $\omega = 2000\,\mathrm{cm}^{-1}$.

electronic band	m_1	m_2	m_3	Ref
effective mass m_i	0.11	0.37	0.33	[79]
k_{F_i}(experiment, $\mathrm{Å}^{-1}$)	0.07	0.28	0.41	[78]
k_{F_i}(theory, unit $0.79\frac{2\sqrt{2}\pi}{a_0}$)	0.41	0.55	0.79	[76]
l_i (nm), from experiments	1.02	4.08	5.97	[78]
l_i (nm), from theory	7.2	2.87	4.6	[76]

k_{F} is the Fermi wave number, m^* is the effective mass of electrons and ω is the angular frequency of the IR photons.

In fact, the information length is not a universal factor representing the system as it depends on the angular frequency, but at a certain value of frequency, it helps to understand the electronic transport inside the nanostructure.

Looking back to the electronic band structure, the indium chains consist of three electron pockets that cross the Fermi level [78]. They have different Fermi wavenumbers k_{F} and different effective masses m^*. According to Ref [79] and [78], the three electron pockets have the effective masses $m_1 = 0.11m$, $m_2 = 0.37m$ and $m_3 = 0.33m$, where m is the rest mass of the electron.

According to the contribution by X. López-Lozano *et al.* [76], the Fermi wave number in these electronic bands are: 0.41, 0.55 and 0.79 respectively, in the unit of $0.79\,\frac{2\sqrt{2}\pi}{a_0}$ where $a_0 = 5.464\,\mathrm{Å}$ is the lattice constant of the bulk silicon crystal.

According to the experimental work by Ahn *et al.* [78], the Fermi wavenumber for the individual bands are 0.07, 0.28 and 0.41 ($\mathrm{Å}^{-1}$).

Table 4.2 shows the estimated information lengths at $\omega = 2000\,\mathrm{cm}^{-1}$ -The latter is the plasmonic absorption frequency of the indium chains which will be shown in the next part. Under one certain excitation regime corresponding to frequency ω, the system shows three different responses associated to individual electron pockets. This difference might contribute optically to the spectroscopic measurements.

To go further with electronic transport in the perpendicular direction, it is necessary to look at the electron density which directly produces optical conductivity. In the sense of the Drude model, the plasma frequencies in the two directions were obtained as $\omega_{\mathrm{P}_{\parallel}} = 48420\,\mathrm{cm}^{-1}$ and $\omega_{\mathrm{P}_{\perp}} = 21705\,\mathrm{cm}^{-1}$ in the chain and interchain direction, respectively. Roughly neglecting the

change in the electron effective mass, according to equation 4.4.2, electron density ratio then can be considered as:

$$\frac{n_{\parallel}}{n_{\perp}} = \frac{m^*_{\parallel}\,\omega^2_{\mathrm{P}_{\parallel}}}{m^*_{\perp}\,\omega^2_{\mathrm{P}_{\perp}}} \sim 4. \tag{4.4.5}$$

In comparison to the Pb film [69] whose information length at frequency $2000\,\mathrm{cm}^{-1}$ is 31 nm, the indium chains presented an information length of one order of magnitude smaller.

In comparison to experimental work by Kanagawa *et al.* [50], the electron mean free path in the chain direction is 6 nm, at the range of information length that has been estimated above.

4.4.2. Plasmonic absorption of indium atom chains at RT

The relative transmittance spectra taken at RT, recorded for different polarization regimes, reflect the anisotropy in the conductivity of the In4×1 chains.

Figure 4.4.3 shows the IR relative transmittance of the chains compared to the bare silicon substrate in the two different directions: parallel and perpendicular. In the chain direction, denoted by $\overline{\Gamma\mathrm{X}}$ in figure 4.4.2, the spectrum shows a strong plasmonic absorption. We observed a broad and resonance-like peak located at around $1700\,\mathrm{cm}^{-1}$ corresponding to an energy of 0.2 eV.

On the other hand, for the perpendicular polarization direction (denoted by $\overline{\mathrm{XM}}$), there is nearly no significant change occurring in the same frequency range - the system is almost transparent, comparable to the bare Si substrate.

Because of the low energy and its strong anisotropy, the observed feature must be related to the one-dimensional metallic behavior of the In chains in accordance to photoelectron spectroscopy [78] and the electronic band calculation (see figure 4.4.2). For polarization parallel to the chains, Drude-type metallic absorption tails from the *dc* to the visible range are expected in case of metallic excitations.

Interestingly, we observed a broad, resonance-like absorption signal centered at $1700\,\mathrm{cm}^{-1}$ (0.2 eV) and vanishing absorption towards lower wavenumbers. The transparent behavior at low wavenumbers and the absorption feature at about 0.2 eV might be attributed to the existence of a small band gap at the Fermi level with about 0.2 eV as the observed feature. However, such assignment contradicts many preceding experiments that showed a non-vanishing density of states at the Fermi level for the RT phase [4].

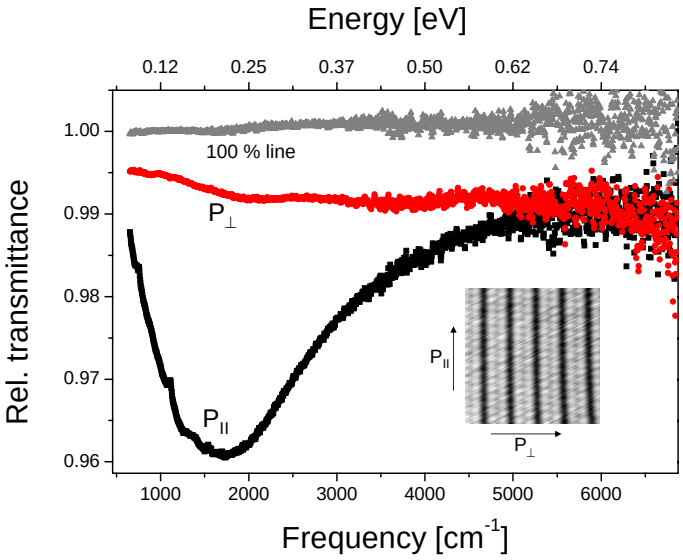

Figure 4.4.3.: The relative IR spectra of In4×1 phase (RT phase). The reference spectra were taken from the bare silicon substrate without indium, at the same polarization conditions. The signal shows strong plasmonic absorption in the chain direction, but it stays nearly transparent in the perpendicular direction. The inset shows the STM measurement of the In4×1 with a scan size of 6 nm×6 nm, tunneling current 20.6 pA, -0.4 μV bias voltage, taken from [75].

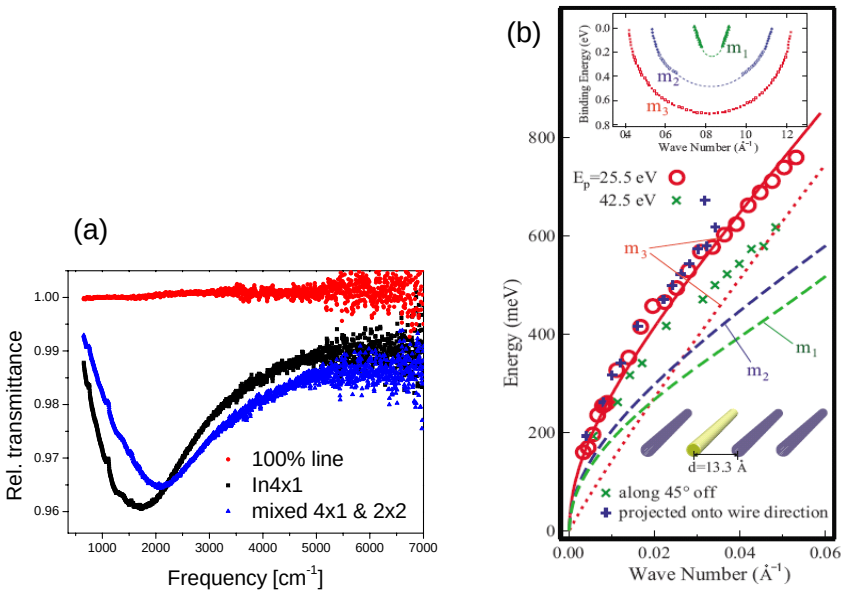

Figure 4.4.4.: The influence of the finite length of indium atom-chains. Left: IR of a sample with a co-existence of In4 × 1 and In2 × 2 in the same domain, which shortened the chain length of the pristine RT phase. Right: Plasmon dispersion obtained by electron energy loss spectroscopy (EELS) on the same system but fabricated in a different apparatus [79].

It is more likely that the observed feature belongs to a low-energy plasmonic excitation in atom wires [79], [3]. In fact, the plasmon dispersion was clearly determined for In atom chains by electron energy loss spectroscopy (EELS) [79]. In this EELS study, the lowest plasmon energy that could be detected separately from elastic reflection is about 150 meV that is excited with a momentum of $q = 0.0033\,\text{Å}^{-1}$. So the chains are at least about 100 nm long in that EELS study. One has to take into account that the rather steep plasmon dispersion curve in Ref. [79] gives strong resonance-energy shifts with slight changes in the wire length L. For example, in Ref. [79], the dispersion relation curve follows an average length of about $L = 55\,\text{nm}$ from the resonance in our IR spectrum at RT, indicating a difference in L due to differences in the crystallinity between the preceding EELS and the present IR studies. For the plasmon wavelength longer than this characteristic chain length, the plasmon wavelength stays at the value for $q = \pi/L$, where a standing wave is formed which allows IR optical detection.

A similar behavior was reported for finite-size Ag particles, namely that below $q < \pi/L$ the plasmonic frequency stays at the value for $q = \pi/L$ [52].

The expected relationship between In chain length L and the IR resonance gets further support from spectra that we measured at less extended In4×1 superstructures with structural disturbances from foreign 2×2 patchy domains where the IR resonance appeared at about 0.25 eV, which corresponds to a mean L of about 48 nm. Our findings on finite metallic chains are in good accordance with the theoretical studies of fundamental plasmon resonances in Na atom chains [80], where a blue shift of the longitudinal mode (polarization parallel to the chain) with decreasing chain length was shown.

The broadness of the plasmonic absorption feature might be attributed to the co-existence of the three different electron bands in the chain direction, as reported experimentally by Ahn *et al.* [78]. Each of them has different information length, ranging from 7.2 nm to 1 nm (see table 4.2). It is worth noticing that due to having this characteristics, indium atom chains are considered of composing three electron pockets whose optical response to IR is varied, producing there the superimpose which broadens the resonance peak.

For polarization perpendicular to the chains, plasmonic excitation (the transverse plasmon mode) is at much higher energies for the same length and has much lower oscillator strength [80]. It is also in agreement with direct measurement of conductivity by Kanagawa *et al.* in Ref [50] where they reported that the conductivity in the chain direction is 60 times higher than in the perpendicular direction. It means also that the indium chains are well-separated leading to the characteristic length in the perpendicular direction is only about 1.3 nm [75]. The standing wave might be formed in this case, since the π/d where d is the width of the chains, is by far smaller than the excitation wavelength.

It is now clear that the observed features in the chain direction is due to the plasmonic absorption along the chains with extremely high plasma frequency and electron density. Because of the well-separation stage in the interchain direction, the standing wave might be formed with much higher energy that does not allow the IRS observation.

4.4.3. Metal to insulator transition

As known from the preceding work by Yeom *et al.* in 1999 [4], the indium atom chains show an instability at low temperatures. The authors reported for the first time on the lattice distortion by electron diffraction as well as photoemission spectroscopy. Here in this work, the lattice distortion is also observed, accompanied by spectroscopic studies in which the full transition from metal to insulator was measured.

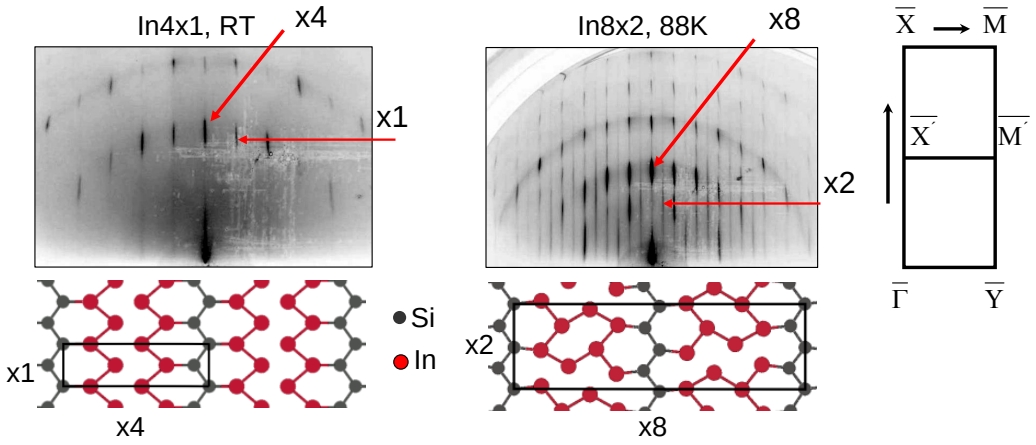

Figure 4.4.5.: Observation of the lattice distortion by electron diffraction. Left: RHEED pattern of In4×1 (RT phase) and its atomic structure with unit cell indicated. Right: In8×2 (LT phase) with the doublicity of the unit cell in the both directions, as seen in the RHEED pattern and atomic structure, taken from [75]. The first Brillouin zone is shown, with the indication of the so-called back-folding of the structure.

Figure 4.4.5 indicates the two electron diffraction patterns of indium atom chains at two different temperatures, at RT and at 88 K. The difference of the RHEED patterns can be identified easily. The In8×2 has some additional diffraction spots in between the fundamental spots of the In4×1 structures.

The atomic structures are also shown with the doublicity of the periodicity in both directions: parallel and perpendicular. The atomic structure at RT shows that each indium wire consists of two indium chains in zigzac shape and the wires are well-separated from each other (in ×4 direction). The silicon chains are beneath the topmost layer isolate interchain connection.

The atomic structure at low temperature shows that in the one hand, the silicon chains are still remained in the pristine shape, but in the other hand, indium chains in one wire are somehow connected to each other. Also, the 8×2 structure reveals that this instability causes the interruption in the chain direction (×2 direction). From this model, it is possible to infer that in the low temperature phase, indium chains are still well-separated and that within one indium wire, the indium atoms are not in the shape of chain any more. A plausible attribution of the metal to insulator transition can be conducted.

Accompanying to the instability, the first Brillouin is also modified from $\bar{\Gamma}\bar{X}\bar{M}\bar{Y}$ to $\bar{\Gamma}\bar{X}'\bar{M}'\bar{Y}$ (not scaled). The shortening of the first BZ is schematically understood by the enlargement of the unit cell in the real space, so-called

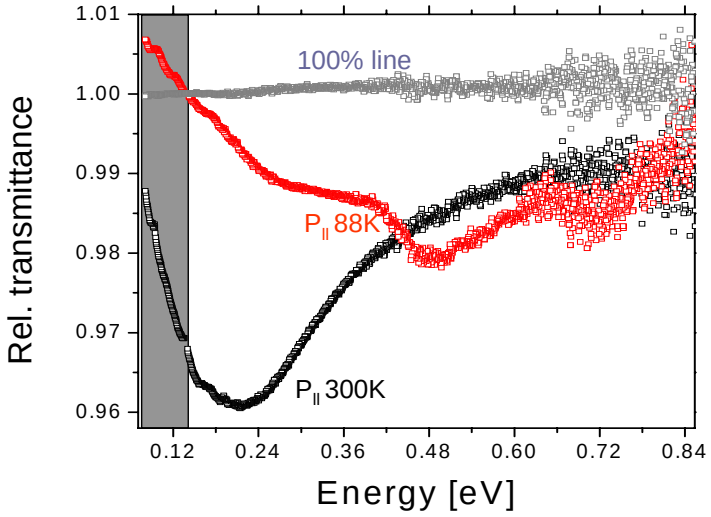

Figure 4.4.6.: Optical detection of the phase transition. The electrical field was directed parallel to the atom-chains at different temperatures, RT and 88 K. The gray rectangular indicates the anti-absorption feature of the In8×2 in comparison to Si(111)-vic at the same temperature.

the back-folding effect.

Figure 4.4.6 compares the spectra of the indium chains for different temperatures with the electric field oriented parallel to the chains. The strong spectral changes are attributed to the phase transition from In4x1 (RT) to In8×2. This transition comes along with a metal-to-insulator transition associated with the periodic lattice distortion, as indicated in Figure 4.4.5.

In comparison to the In4×1, the In8×2 phase does not show the strong and broad plasmonic feature around 0.2 eV, but a weaker and broader peak at about 0.26 eV instead. Two new significant absorption peaks arise at 0.48 eV and 0.72 eV.

Figure 4.4.7 provides a better understanding about the In8×2 phase for the two different polarization directions. The two spectra are only slightly different, meaning that the anisotropy of the system has almost vanished, in good accordance with the work by Kanagawa *et al.* [50]. Besides, three absorption peaks arise for polarization in the chain parallel direction.

Below 0.15 eV it can be seen that the In8×2 structure for both the polarization directions is more transparent than the silicon bare surface. This is a strong indication for the insulating character of the In8×2 surface since the reconstructed silicon surface has metallic Si dangling bonds of surface states [42].

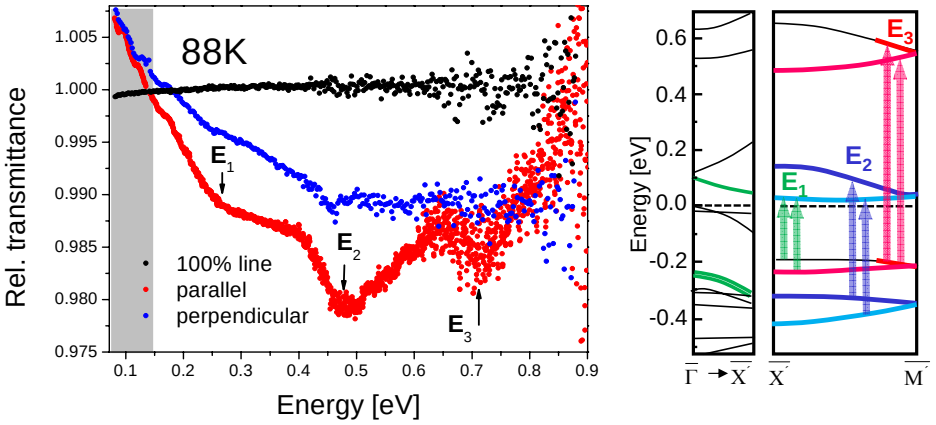

Figure 4.4.7.: Possible assignments for the absorption peaks resulting from the structural phase transition, accompanied with a gap opening. Left: Relative transmittance spectra in the two excitation regimes: parallel and perpendicular to the chains. The gray rectangular shows the anti-absorption feature taking place at energies smaller than 0.15 eV. Right: band structure calculation with some possible optical transitions that can be assigned to the interband transitions E_1, E_2 and E_3. The smallest energy transition E_1 is related to the opened gap.

The right hand side of Figure 4.4.7 shows the calculated band structure using the SIESTA code [13] for the In chains on a 5-bilayers Si slab with a k-sampling equivalent to 256 k-points in the (1×1) unit cell [9]. The large number of k-points and relatively thick slabs are crucial to converge the results [75].

In Figure 4.4.7, the transition E_2 (0.48 eV) and E_3 (0.72 eV) are assigned to the interband transition from the nearly-parallel bands close to the Fermi level and along the direction (see inset). These two absorption peaks are in good accordance with a recent work by Chandola *et al.* using infrared ellisometry[81].

In figure 4.4.7, we make a tentative assignment in which E_1 is related to the transitions giving rise to the peak at 0.26 eV and E_2 with those behind the feature at 0.37 eV. However, in the calculations, contrary to the experiment, these two peaks have very similar intensities and widths. This discrepancy can be due to the limitations of density functional calculations or might be related to the uncertainties introduced by the observed preparation dependence of E_1.

In the experimental spectra, the absorption structure at 0.26 eV (E_1) is

[9] Calculation performed at the group of Prof. D. S. Portal. To make the explanation comprehensively, a short description is paragraphed here

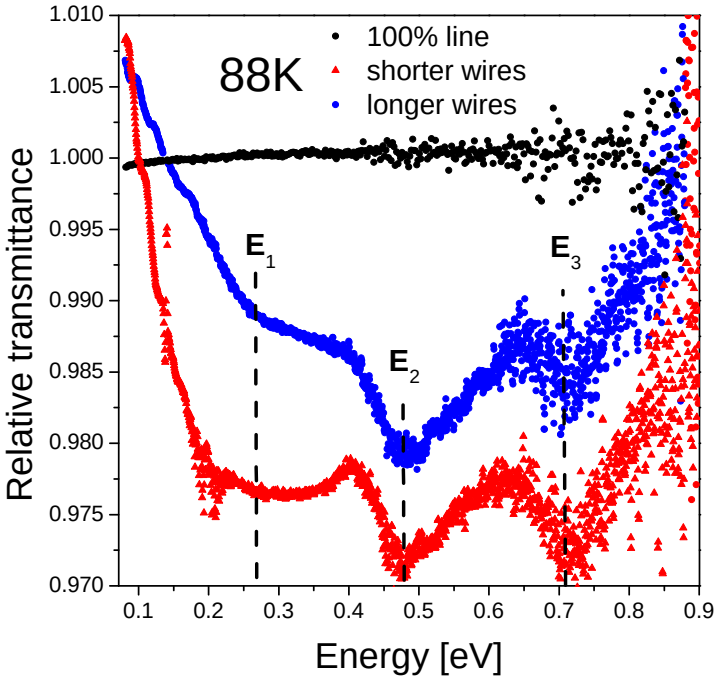

Figure 4.4.8.: Dependency of sample preparation on the metal to insulator transition of indium wires. The longer wires were obtained when a new sample holder was introduced to improve the surface quality during flashing process, therefore in this case the sample was not distorted after performing experiments. Data courtesy by Dr. T. Nagao and Dr. G. Han, from MANA, NIMS, Japan.

either a rather broad peak or only a shadow. We found typical values between 0.2 and 0.3 eV. The spectral position compares well with features of the tunneling spectrum of Ref. [82], [83].

In a recent work by Chandola *et al.* [81], there was the lowest excitation feature published for the reflectance measurements located at 0.35 eV. In comparison to that work, our peak position E_1 has a smaller energy.

As can be seen at the calculation result in Figure 4.4.7, transition near $\overline{\Gamma}$ point is slightly larger than the observed value of E_1. But it will give the same kind of broad feature near 0.3 eV because of the less parallelity of the bands. It should be noted that the position of the maximum absorption of E_1 depends on preparation details that can introduce imperfections by defects at the structural phases. Indeed, the calculation shows that the band structure of this low-dimensional system is extraordinarily dependent on fine structural details.

In summary, an optical detection of the indium atom wires (or chains, in some cases) has been realized. At the RT phase, In wires show a plasmonic absorption along the wire direction but not in the interchain direction. This effect is related to the strongly metallic character of this system, showing also the correlation with the electron energy loss spectroscopy.

At low temperature phase, In wires shows a phase transition from metal to insulator accompanying by a lattice distortion. This transition opens up a new gap and two interband transitions which all are visible in our experiments.

5. Conclusions

5.1. Conclusions

Within framework of this thesis, one-dimensional metallic nanostructures grown by self-organization method on silicon vicinal surfaces have been investigated by means of infrared spectroscopy. The main points of this work can be summarized as following:

1. The preparation of the silicon surface by the resistive heating method has been optimized with a reliable procedure. STM images of the Si(557) surfaces indicate the perfect grating-like structure which is ideally suitable for lead to grow. Annealing at 830°C for 15 min allows us to enlarge the domain size of the reconstructed structure of Si(557) which later is of important to fabricate huge, homogeneous areas of lead nanowires. Also, STM and RHEED studies on gold chains on Si(557) reveal the co-existence of gold chains and silicon chains on one terrace. RHEED diffraction patterns indicate that the periodicity of silicon chains is two times higher than that of gold. IR studies of Au/Si(557) show that the gold chains are absolutely transparent, in comparison to the silicon substrate.

2. For the data of lead growth: the *in-situ* observation during lead growth was established. The shift of the resonance frequency to lower wavenumbers indicates the development in length of the nanowires versus coverage. There was a good agreement of the experimental data with the description by the optical antenna theory.

3. As the growth of lead nanowires is a far from equilibrium process, when the nucleation stops, the as-synthesized nanowires start to relax, leading to shorter wires, as observed under parallel excitation regime. More importantly, the average length of the nanowires can be controlled by governing four experimental parameters; namely: lead coverage, substrate temperature, flux and substrate reconstruction.

4. Beyond cooling, the nanowires show a decrease of relative transmittance, meaning also the increase of the extinction cross section of the single nanowire at low temperature. There was no shift of the resonance frequencies due to low temperature obtained so far. Nearly the same decreasing behavior of relative transmittance was obtained for every coverage, ranging from 2 ML to 10 ML. In addition, the plasmon linewidth (FWHM) of the normalized extinction cross section versus temperature indicates a similar tendency to the decrease of relative transmittance. In general, the decrease of plasmon linewidth was about 27 % for the case of 3 ML. The reason for the decrease of FWHM at low temperature can be attributed to the reduction of electron-phonon scattering. The other scattering events such as electron-electron, electron-surface, and radiation damping are temperature independent. The discrepancy between experimental data and theoretical estimation might be attributed to the nature of the plasmonic broadening due to the size distribution of nanowires as well as to a contribution from the other scattering events.

5. The experimental data on indium atom chains at RT shows a strong plasmonic absorption in the chain direction, but it was nearly transparent in the interchain direction. The broadness of the plasmonic absorption at RT can be attributed to the superimposing of three electron pockets that have different information lengths in the Fermi surface. At 88 K the system shows a phase transition which is observed by RHEED. Accompanying to that, the IR spectrum shows an absorption peak related to the gap opening at around 0.26 meV and two new interband absorptions peaks.

Bibliography

[1] Jer-Shing Huang, Thorsten Feichtner, Paolo Biagioni, and Bert Hecht. Impedance matching and emission properties of nanoantennas in an optical nanocircuit. *Nano Letters*, 9 (5):1897, 2009.

[2] Frank Neubrech, Annemarie Pucci, Thomas Walter Cornelius, Shafqat Karim, Aitzol García-Etxarri, and Javier Aizpurua. Resonant plasmonic and vibrational coupling in a tailored nanoantenna for infrared detection. *Phys. Rev. Lett.*, 101:157403, 2008.

[3] Nagao Tadaaki, Yaginuma Shin, Inaoka Takeshi, and Sakurai Toshio. One-dimensional plasmon in an atomic-scale metal wire. *Phys. Rev. Lett.*, 97:116802, 2006.

[4] H. W. Yeom, S. Takeda, E. Rotenberg, I. Matsuda, K. Horikoshi, J. Schaefer, C. M. Lee, S. D. Kevan, T. Ohta, T. Nagao, and S. Hasegawa. Instability and charge density wave of metallic quantum chains on a silicon surface. *Phys. Rev. Lett.*, 82:4898, 1999.

[5] M. Jałochowski and E. Bauer. Growth of metallic nanowires on anisotropic Si substrates: Pb on vicinal Si(001), Si(755), Si(533) and Si(110). *Surface Science*, 480:109, 2001.

[6] Gerhard Fahsold and Annemarie Pucci. *Non-contact Measurement of Thin-Film Conductivity by ir Spectroscopy*, chapter Advances in Solid State Physics, pages 833–847. Springer Verlag, Berlin/Heidelberg, 2003.

[7] Robert Lovrinčić and Annemarie Pucci. Infrared optical properties of chromium nanoscale films with a phase transition. *Phys. Rev. B*, 80:205404, 2009.

[8] Fanzeng Meng. *IR Spectroscopy Studies of Silver and Copper Nano-films*. PhD thesis, Heidelberg University, 2007.

[9] Dominik Enders. *Surface Enhanced Infrared Absorption on Au Nanoparticle Films for Optical Biosensing*. PhD thesis, Heidelberg University, 2006.

[10] Somendra M. Bhattacharjee and Sutapa Mukherji. Vicinal surfaces, fractional statistics, and universality. *Phys. Rev. Lett.*, 83:2374, 1999.

[11] J.K. Mackenzie, A.J.W. Moore, and J.F. Nicholas. Bonds broken at atomically flat crystal surfaces–i: Face-centred and body-centred cubic crystals. *Journal of Physics and Chemistry of Solids*, 23:185, 1962.

[12] R. J. Phaneuf and Ellen D. Williams. Surface phase separation of vicinal si(111). *Phys. Rev. Lett.*, 58(24):2563, Jun 1987.

[13] J. N. Crain, J. L. McChesney, Fan Zheng, M. C. Gallagher, P. C. Snijders, M. Bissen, C. Gundelach, S. C. Erwin, and F. J. Himpsel. Chains of gold atoms with tailored electronic states. *Phys. Rev. B*, 69:125401, 2004.

[14] I. K. Robinson, P. A. Bennett, and F. J. Himpsel. Structure of quantum wires in Au/Si(557). *Phys. Rev. Lett.*, 88:096104, 2002.

[15] P. Segovia, D. Purdie, M. Hengsberger, and Y. Baer. Observation of spin and charge collective modes in one-dimensional metallic chains. *Nature*, 402:504, 1999.

[16] M. Schock, C. Surgers, and H. v. Lohneysen. Atomically resolved tunneling spectroscopy on Si(557)-Au. *EPL (Europhysics Letters)*, 74:473, 2006.

[17] I. Barke, Fan Zheng, T. K. Rügheimer, and F. J. Himpsel. Experimental evidence for spin-split bands in a one-dimensional chain structure. *Phys. Rev. Lett.*, 97:226405, 2006.

[18] M. Klevenz, F. Neubrech, R. Lovrincic, M. Jałochowski, and A. Pucci. Infrared resonances of self-assembled Pb nanorods. *Applied Physics Letters*, 92:133116, 2008.

[19] T. W. Ebbesen, H. J. Lezec, H. F. Ghaemi, T. Thio, and P. A. Wolff. Extraordinary optical transmission through sub-wavelength hole arrays. *Nature*, 391:667, 1998.

[20] J. Aizpurua, Garnett W. Bryant, Lee J. Richter, F. J. García de Abajo, Brian K. Kelley, and T. Mallouk. Optical properties of coupled metallic nanorods for field-enhanced spectroscopy. *Phys. Rev. B*, 71:235420, 2005.

[21] H. A. Atwater. The promise of plasmonics. *Sci. Am*, 296:56, 2007.

[22] Lukas Novotny. Effective wavelength scaling for optical antennas. *Phys. Rev. Lett.*, 98:266802, 2007.

[23] Feng Wang and Y. Ron Shen. General properties of local plasmons in metal nanostructures. *Phys. Rev. Lett.*, 97:206806, 2006.

[24] N. W. Ashcroft and N. D. Mermin. *Solid State Physics*. Saunders, College Publishing, Orlando, 1976.

[25] U. Fano. Effects of configuration interaction on intensities and phase shifts. *Phys. Rev.*, 124(6):1866, Dec 1961.

[26] F. Neubrech, T. Kolb, R. Lovrincic, G. Fahsold, A. Pucc, J. Aizpurua, T. W. Cornelius, M. E. Toimil-Molares, R. Neumann, and S. Karim. Resonances of individual metal nanowires in the infrared. *Appl. Phys. Lett. 89, 253104 (2006)*, 253104:89, 2006.

[27] Markus Klevenz. Optische Eigenschaften von Blei-Nanodrähten auf Si(335)/Au. Diplomarbeit, Ruprecht-Karls-Universität Heidelberg, 2006.

[28] A. A. Saranin V. G. Lifshits and A. V. Zotov. *Surface Phases on Silicon: Preparation, Structures, and Properties*. John Wiley & Sons, 1994.

[29] Florian Kost. Präparation von dünnen Filmen und Nanodrähten aus Blei und deren Analyse mittels IR-Spektroskopie. Diplomarbeit, Universität Heidelberg, 2005.

[30] M. Jałochowski, M. Hoffmann, and E. Bauer. Pb layer-by-layer growth at very low temperatures. *Phys. Rev. B*, 51:7231, 1995.

[31] Ayahiko Ichimya and Philip L. Cohen. *Reflection High Energy Electron Diffraction*. Cambridge University Press, 2004.

[32] Kunio Takayanagi, Yasumasa Tanishiro, Shigeki Takahashi, and Masaetsu Takahashi. Structure analysis of Si(111)-7×7 reconstructed surface by transmission electron diffraction. *Surface Science*, 164:367, 1985.

[33] Y. L. Wang, H.-J. Gao, H. M. Guo, H. W. Liu, I. G. Batyrev, W. E. McMahon, and S. B. Zhang. Tip size effect on the appearance of a stm image for complex surfaces: Theory versus experiment for Si(111)–(7×7). *Phys. Rev. B*, 70:073312, 2004.

[34] G. Binnig, C. F. Quate, and Ch. Gerber. Atomic force microscope. *Phys. Rev. Lett.*, 56:930, 1986.

[35] Shuji Hasegawa, Xiao Tong, Sakura Takeda, Norio Sato, and Tadaaki Nagao. Structures and electronic transport on silicon surfaces. *Progress in Surface Science*, 60:89, 1999.

[36] J. Viernow, J.-L. Lin, D. Y. Petrovykh, F. M. Leibsle, F. K. Men, and F. J. Himpsel. Regular step arrays on silicon. *Applied Physics Letters*, 72:948, 1998.

[37] R. J. Phaneuf and Ellen D. Williams. Step-height-tripling transition on vicinal Si(111). *Phys. Rev. B*, 41:2991, 1990.

[38] T. Nagao. Private conversation.

[39] Ye-Chuan Xu and Bang-Gui Liu. Two-speed phase dynamics in the Si(111) $(7 \times 7) - (1 \times 1)$ phase transition. *Phys. Rev. Lett.*, 100:056103, 2008.

[40] H. V. Chung, M. Klevenz, R. Lovrincic, F. Neubrech, O. Skibbe, A. Pucci, P. Nita, M. Jałochowski, and Tadaaki Nagao. Studies on gold atom chains and lead nanowires on silicon vicinal surfaces. *Journal of Physics: Conference Series*, 187:012025, 2009.

[41] A. Kirakosian, R. Bennewitz, J. N. Crain, Th. Fauster, J.-L. Lin, D. Y. Petrovykh, and F. J. Himpsel. Atomically accurate Si grating with 5.73 nm period. *Applied Physics Letters*, 79:1608, 2001.

[42] C Tejedor, F Flores, and E Louis. Correlation and electron-phonon effects in the (111)-silicon dangling-bond surface states. *Journal of Physics C: Solid State Physics*, 19:543, 1986.

[43] R Bennewitz, J N Crain, A Kirakosian, J-L Lin, J L McChesney, D Y Petrovykh, and F J Himpsel. Atomic scale memory at a silicon surface. *Nanotechnology*, 13:499, 2002.

[44] Tsuyoshi Hasegawa and Shigeyuki Hosoki. Intrarow diffusion of Au atoms in the Si(111)-(5×2)Au structure. *Phys. Rev. B*, 54:10300, 1996.

[45] Pil-Gyu Kang, Jin Sung Shin, and Han Woong Yeom. Point defects along metallic atomic wires on vicinal Si surfaces: Si(557)-Au and Si(553)-Au. *Surface Science*, 603:2588, 2009.

[46] M. Krawiec, T. Kwapiński, and M. Jałochowski. Double nonequivalent chain structure on a vicinal Si(557)-Au surface. *Phys. Rev. B*, 73:075415, 2006.

[47] Canhua Liu, Takeshi Inaoka, Shin Yaginuma, Tomonobu Nakayama, Masakazu Aono, and Tadaaki Nagao. The excitation of one-dimensional plasmons in si and au-si complex atom wires. *Nanotechnology*, 19(35):355204, 2008.

[48] Steven C. Erwin, Ingo Barke, and F. J. Himpsel. Structure and energetics of Si(111)-(5x2)-Au. *Phys. Rev. B*, 80(15):155409, Oct 2009.

[49] Shuji Hasegawa. Transport at atomic wires on silicon surfaces. In *DPG meeting Berlin 2008*, 2008.

[50] Taizo Kanagawa, Rei Hobara, Iwao Matsuda, Takehiro Tanikawa, Akiko Natori, and Shuji Hasegawa. Anisotropy in conductance of a quasi-one-dimensional metallic surface state measured by a square micro-four-point probe method. *Phys. Rev. Lett.*, 91:036805, 2003.

[51] Hiroyuki Okino, Iwao Matsuda, Shiro Yamazaki, Rei Hobara, and Shuji Hasegawa. Transport in defective quasi-one-dimensional arrays of chains of gold atoms on a vicinal silicon surface. *Phys. Rev. B*, 76(3):035424, Jul 2007.

[52] F. Moresco, M. Rocca, T. Hildebrandt, and M. Henzler. Plasmon confinement in ultrathin continuous Ag films. *Phys. Rev. Lett.*, 83:2238, 1999.

[53] H. Brune. Microscopic view of epitaxial metal growth: nucleation and aggregation. *Surface Science Reports*, 31:121, 1998.

[54] M. Jałochowski and E. Bauer. Self-assembled parallel mesoscopic Pb-wires on Au-modified Si(533) substrates. *Progress in Surface Science*, 67:79, 2001.

[55] Kedong Wang, Xieqiu Zhang, M.M.T. Loy, and Xudong Xiao. The role of Pb wetting layer conduction in tunneling spectroscopy of Pb nanoislands on Si(111) surface. *Surface Science*, 602:1217, 2008.

[56] Yoshihito Maeda. Visible photoluminescence from nanocrystallite ge embedded in a glassy SiO_2 matrix: Evidence in support of the quantum-confinement mechanism. *Phys. Rev. B*, 51:1658, 1995.

[57] Gwyddion. `http://gwyddion.net/`.

[58] M. A. Ordal, L. L. Long, R. J. Bell, S. E. Bell, R. R. Bell, Jr. R. W. Alexander, and C. A. Ward. Optical properties of the metals Al, Co, Cu, Au, Fe, Pb, Ni, Pd, Pt, Ag, Ti, and W in the infrared and far infrared. *Appl. Opt.*, 22:1099, 1983.

[59] A. M. Ionov A. N. Myagkov A. N. Chaika, S. I. Bozhko and N. V. Abrosimov. Stm and leed studies of atomically ordered terraced Si(557) surfaces. *Semiconductors*, 41:431, 2007.

[60] A. N. Chaika, D. A. Fokin, S. I. Bozhko, A. M. Ionov, F. Debontridder, V. Dubost, T. Cren, and D. Roditchev. Regular stepped structures on clean Si(hhm)7×7 surfaces. *Journal of Applied Physics*, 105:034304, 2009.

[61] J A Venables, G D T Spiller, and M Hanbucken. Nucleation and growth of thin films. *Reports on Progress in Physics*, 47:399, 1984.

[62] M. V. Ramana Murty. Morphological stability of nanostructures. *Phys. Rev. B*, 62(24):17004, Dec 2000.

[63] Margret Giesen. Step and island dynamics at solid/vacuum and solid/liquid interfaces. *Progress in Surface Science*, 68:1, 2001.

[64] Yinggang Li, M. C. Bartelt, J. W. Evans, N. Waelchli, E. Kampshoff, and K. Kern. Transition from one- to two-dimensional island growth on metal (110) surfaces induced by anisotropic corner rounding. *Phys. Rev. B*, 56:12539, 1997.

[65] Mingzhao Liu, Matthew Pelton, and Philippe Guyot-Sionnest. Reduced damping of surface plasmons at low temperatures. *Phys. Rev. B*, 79:035418, 2009.

[66] Bradley J. Frey, Douglas B. Leviton, and Timothy J. Madison. Temperature-dependent refractive index of silicon and germanium. volume 6273, page 62732J. SPIE, 2006.

[67] W. E. Lawrence and J. W. Wilkins. Electron-electron scattering in the transport coefficients of simple metals. *Phys. Rev. B*, 7:2317, Mar 1973.

[68] T. Holstein. Theory of transport phenomena in an electron-phonon gas. *Annals of Physics*, 29:410, 1964.

[69] Annemarie Pucci, Florian Kost, Gerhard Fahsold, and Mieczyslaw Jałochowski. Infrared spectroscopy of Pb layer growth on Si(111). *Phys. Rev. B*, 74:125428, 2006.

[70] Debye temperature. `http://chemistry.about.com/od/elementfacts/a/lead.htm`.

[71] R. B. Dingle. The electrical conductivity of thin wires. *Proc. R. Soc. Lond. A*, 201:545, 1950.

[72] C. Sönnichsen, T. Franzl, T. Wilk, G. von Plessen, J. Feldmann, O. Wilson, and P. Mulvaney. Drastic reduction of plasmon damping in gold nanorods. *Phys. Rev. Lett.*, 88:077402, 2002.

[73] U. Kreibig and M. Vollmer. *Optical Properties of Metal Clusters*. Springer, Berlin, 1995.

[74] Feng Wang and Y. Ron Shen. General properties of local plasmons in metal nanostructures. *Phys. Rev. Lett.*, 97:206806, Nov 2006.

[75] H. V. Chung, C. J. Kubber, G. Han, S. Rigamonti, D. Sanchez-Portal, D. Enders, A. Pucci, and T. Nagao. Optical detection of electronic excitations in 1 nm-wide atomic wires. *Applied Physics Letters, submitted*, 2010.

[76] X. López-Lozano, A.A. Stekolnikov, J. Furthmüller, and F. Bechstedt. Band structure and electron gas of In chains on Si(111). *Surface Science*, 589:77, 2005.

[77] M. J. Jory J. R. Sambles, A. P. Hibbins and Azizbekyan. A surface plasmon study of the optical dielectric function of indium. *J. Mod. Opt.*, 47:1227, 2000.

[78] J. R. Ahn, J. H. Byun, H. Koh, E. Rotenberg, S. D. Kevan, and H. W. Yeom. Mechanism of gap opening in a triple-band peierls system: In atomic wires on Si. *Phys. Rev. Lett.*, 93:106401, 2004.

[79] Canhua Liu, Takeshi Inaoka, Shin Yaginuma, Tomonobu Nakayama, Masakazu Aono, and Tadaaki Nagao. Disappearance of the quasi-one-dimensional plasmon at the metal-insulator phase transition of indium atomic wires. *Phys. Rev. B*, 77:205415, 2008.

[80] Jun Yan, Zhe Yuan, and Shiwu Gao. End and central plasmon resonances in linear atomic chains. *Phys. Rev. Lett.*, 98:216602, 2007.

[81] S. Chandola, K. Hinrichs, M. Gensch, N. Esser, S. Wippermann, W. G. Schmidt, F. Bechstedt, K. Fleischer, and J. F. McGilp. Structure of Si(111)-in nanowires determined from the midinfrared optical response. *Phys. Rev. Lett.*, 102:226805, 2009.

[82] C. González, Jiandong Guo, J. Ortega, F. Flores, and H. H. Weitering. Mechanism of the band gap opening across the order-disorder transition of Si(111)(4×1)-in. *Phys. Rev. Lett.*, 102:115501, 2009.

[83] S. J. Park, H. W. Yeom, S. H. Min, D. H. Park, and I. W. Lyo. Direct evidence of the charge ordered phase transition of indium nanowires on Si(111). *Phys. Rev. Lett.*, 93:106402, 2004.

6. Acknowlegements

I would like to express my sincerest appreciation to my adviser, Prof. Dr. Annemarie Pucci for her support to me in getting the scholarship and giving me opportunity to pursue PhD studies here in Germany. Main important points of this thesis are guided by her as a "Doktormutter" so that without her supervision, this thesis has not been established.

I also would like to acknowledge Priv. Doz. Maarten F.M. DeKieviet for his willingness to be second referee of this thesis.

I am grateful to Prof. Dr. M. Jałochowski and Dr. T. Nagao for their hospitality of my visits, for considering me as one of their students, for inducting me into the experiment's voodoo.

I wish to thank Dr. Olaf Skibbe and Dr. Robert Lovrincic for their critical proof reading, comments and encouragement.

I also wish to thank all of my current and former group members for their contributions to the setup of the system; for their share not only in scientific knowledge, but also in the private life. Special thanks go to: Dr. Markus Klevenz, Dr. Frank Neubrech, Steffen Wetzel, Daniel Weber, Jörg Bochterle. I wish to acknowledge Pawel Nita (Lublin), Dr. Han Gui and Dr. Osamu Saito (Tsukuba) for their co-operation during my visits to their institutions. I would like to take this chance to appreciate the contribution of the mechanical and electronics workshops as well. The user community of open software *Gwydion* and *imageJ* is gratefully acknowledged.

I would like to acknowledge the fellowship program of the Gottlieb Daimler and Karl Benz foundation. I wish also to thank the financial contribution of the Heidelberg Graduate School of Fundamental Physics.

Special thanks to my big family, for putting on me their belief, love and never ending encouragement.

Declaration: I hereby confirm that I wrote this thesis on my own and that I did not use other sources or means than stated.

Heidelberg, the Signature

A. Appendix

A.1. RHEED of Au/Si(557), different coverage

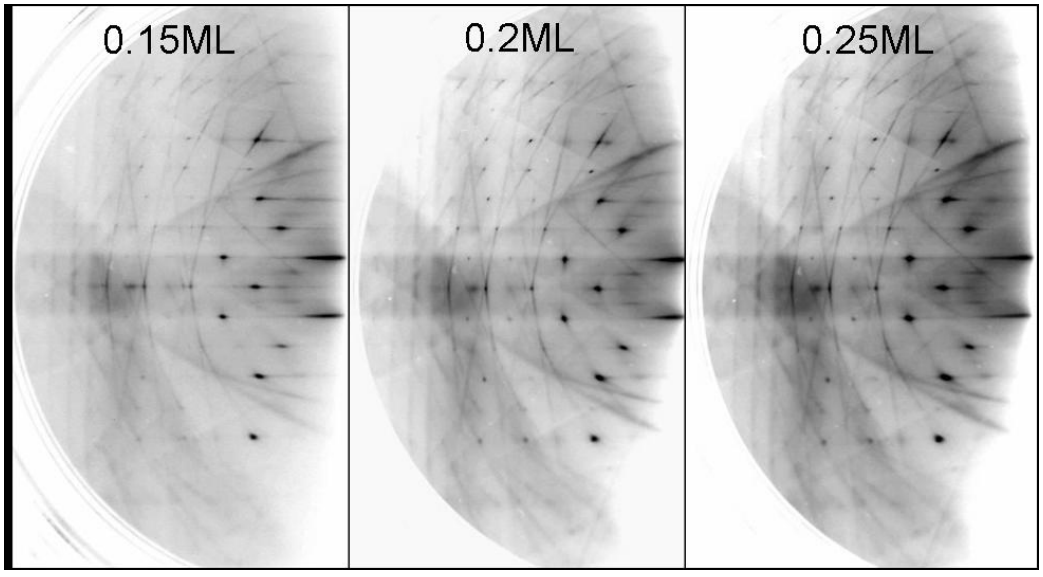

Figure A.1.1.: RHEED patterns of Au-Si(557) with different coverage.

A.2. Stability of nanowires in ambient conditions

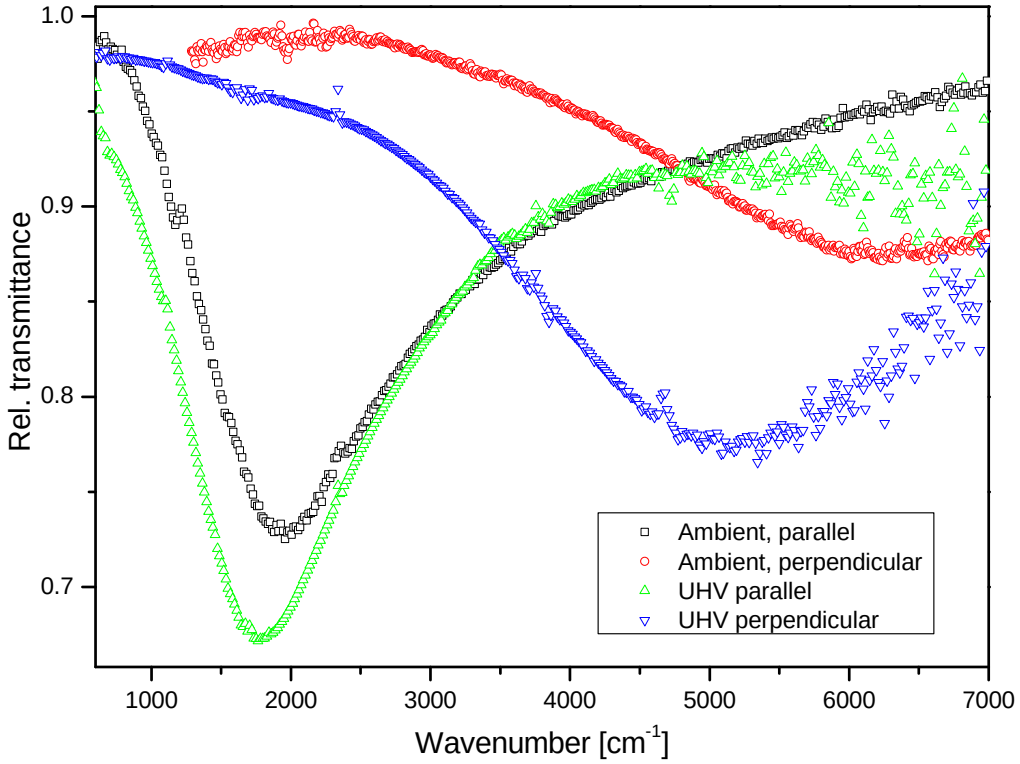

Figure A.2.1.: A comparison of the plasmonic absorption of 10 ML of Pb nanoantenna in vacuum and in air. Data in the ambient conditions was taken after 45 hours since transferring sample to air. Data courtesy of M. Klevenz and F. Neubrech, KIP.

A.3. RHEED diffraction patterns of the different surface reconstructions on Si(111)

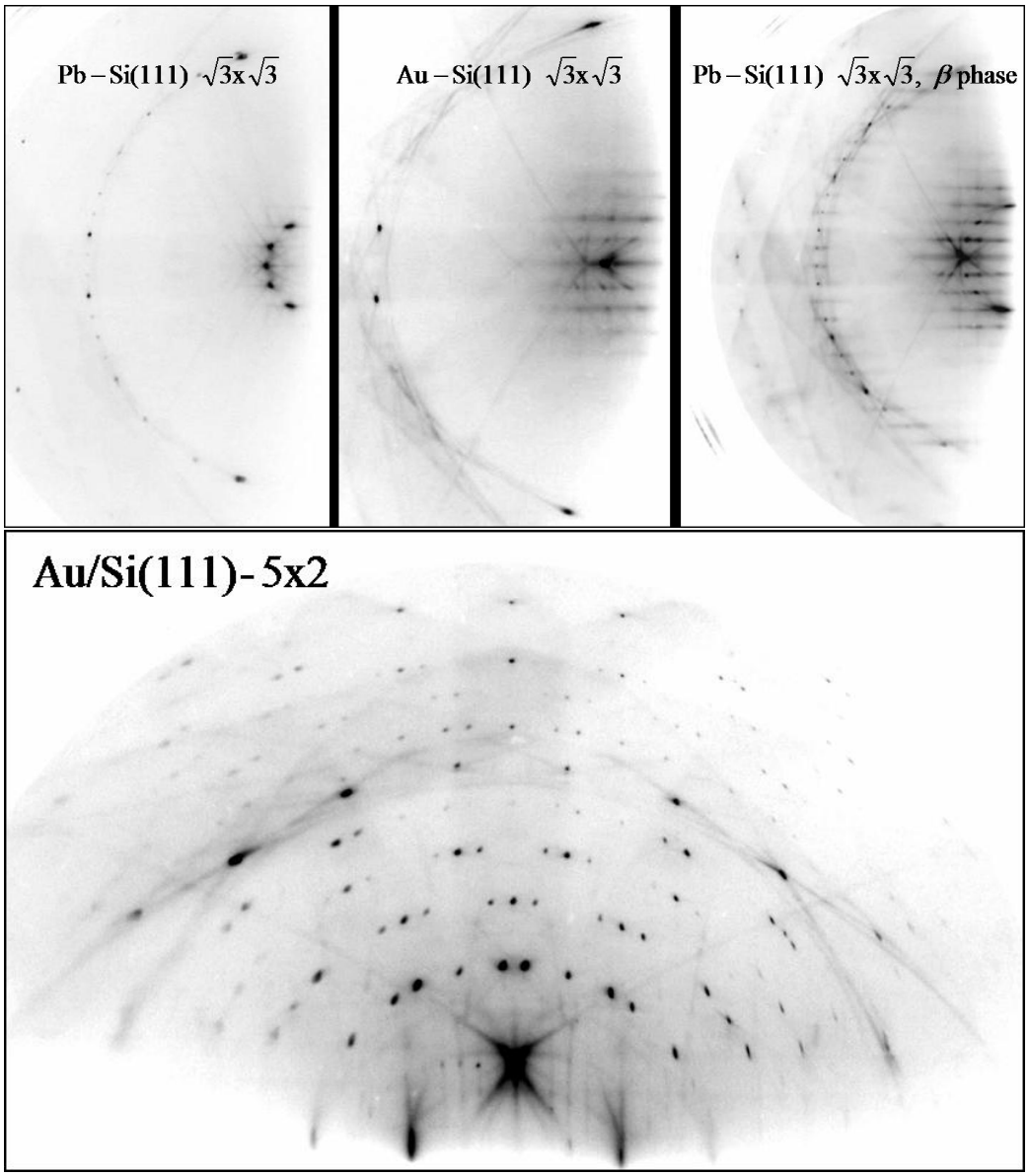

Figure A.3.1.: RHEED Reconstructions on Si(111) with detail of notation for each surface.